SANDIA REPORT
SAND2005-7083
Unlimited Release
Printed December 2005

MEMS Characterization LDRD

Final Report (FY03–FY05)

Steven M. Thornberg, Jason R. Brown, Kevin R. Zavadil, James A. Ohlhausen, David R. Tallant, Manuel J. Garcia, Regina L. Simpson, Michael S. Kent, and Therese A. Ordonez

Prepared by
Sandia National Laboratories
Albuquerque, New Mexico 87185 and Livermore, California 94550

Sandia is a multiprogram laboratory operated by Sandia Corporation, a Lockheed Martin Company, for the United States Department of Energy's National Nuclear Security Administration under Contract DE-AC04-94AL85000.

Sandia National Laboratories

Issued by Sandia National Laboratories, operated for the United States Department of Energy by Sandia Corporation.

Available to DOE and DOE contractors from
U.S. Department of Energy
Office of Scientific and Technical Information
P.O. Box 62
Oak Ridge, TN 37831

Telephone: (865) 576-8401
Facsimile: (865) 576-5728
E-Mail: reports@adonis.osti.gov
Online ordering: http://www.osti.gov/bridge

Available to the public from
U.S. Department of Commerce
National Technical Information Service
5285 Port Royal Rd.
Springfield, VA 22161

Telephone: (800) 553-6847
Facsimile: (703) 605-6900
E-Mail: orders@ntis.fedworld.gov
Online order: http://www.ntis.gov/help/ordermethods.asp?loc=7-4-0#online

SAND2005-7083
Unlimited Release
Printed December 2005

MEMS Characterization LDRD Final Report (FY03-FY05)

Steven M. Thornberg, Jason R. Brown
Materials Reliability

Michael S. Kent
Biomolecular Analysis & Imaging

Kevin R. Zavadil
Corrosion & Electrochemical Sciences

Therese A. Ordonez
Product/Process Development Value Stream

James A. Ohlhausen, David R. Tallant,
Manuel J. Garcia, Regina L. Simpson
Materials Characterization

Sandia National Laboratories
PO Box 5800, MS0889
Albuquerque, NM 87185

Abstract

Chemical and physical materials-aging processes can significantly degrade the long-term performance and reliability of dormant microsystems, which results from materials interactions that changes both bulk and interfacial properties. The goal was to develop a set analytical strategies and methods to measure the gas and spatially resolved surface chemical inventories in microelectromechanical systems (MEMS).

Time-of-flight secondary ion mass spectrometric (TOF-SIMS) methods were developed to quantify the surface coverage of self-assembled monolayers (SAMs) and generate a unique chemical signature that indicated local SAM displacement. Sophisticated algorithms were developed to extract the useful information from these very large data sets. X-ray-induced photoelectron emission spectroscopy (XPS) was used to generate the absolute quantitation of SAMS surface coverage that was used to calibrate the TOF-SIMS measurements. Atomic force microscopy (AFM) and scanning Kelvin force microscopy (SKFM) techniques were used to investigate subtle variations in the silane surface film produced by tribological wear. Attenuated total reflectance infrared spectroscopy (ATR-IR) was used to explore the structure of VSAM-deposited molecules in a MEMS-like environment. Additionally, methods for the fluorescent tagging of molecules were developed and demonstrated.

Finally, methods were developed to determine the hermeticity of MEMS packages using gas analyses. Methods developed are radically different from standard techniques because of the custom hardware used and the pulsed method for gas introduction into the residual gas analyzer. This change enables not only the analysis of nanoliter-sized MEMS packages, but also a rapid way to analyze the gases repetitively in a statistically significant manner (e.g., gas from each package was analyzed dozens of times during a 20 minute time period).

TABLE OF CONTENTS

List of Figures

List of Tables

1. NANOLITER MEMS PACKAGE GAS SAMPLING TO DETERMINE HERMETICITY

1.1. Introduction

Maintaining the integrity of the internal atmosphere of a hermetic device is essential for long-term component reliability because it is within this environment that all internal materials age. Characterization of the internal atmosphere is of great importance to materials aging modeling. As the size of MEMS packages decrease with miniaturization, characterization of the internal atmosphere becomes increasingly difficult. Typical transistor metal cans (e.g., TO-5 type) and large MEMS devices have an internal volume of tenths of a milliliter or more. Such devices have been sampled routinely for years using existing technologies (1-4). Last year, gas-sampling methods for smaller-sized MEMS packages were developed and successfully demonstrated on packages having internal volumes as low as 3 microliters (package outside dimensions: ~1 x 2 x 5 mm). Results from those sampling efforts showed most of the devices that are sealed with anodic bonds remained hermetic with the major variation in gas concentration being hydrogen, ranging from 1% to 10% by volume in concentration. One of the limitations of most of these analyses is that the gas sample is consumed rapidly and multiple analyses on a single sample are difficult. The disadvantage of having to rely on a single measurement for the various gas species is that it precludes any statistical analysis of the data for assessing confidence.

In this paper, we present results on a recently developed technique that allow us to reliably sample MEMS devices having internal volumes of 30 nanoliters (Figure 1). Not only is the sample analyzed, but also multiple measurements are obtained for each gas species. This sample can be further analyzed for extended periods of time (tens of minutes to hours). This significant jump in capability is made possible through a combination of volume reduction, incorporation of solid-state pressure sensor, and a modified all-metal bellows-sealed sampler valve.

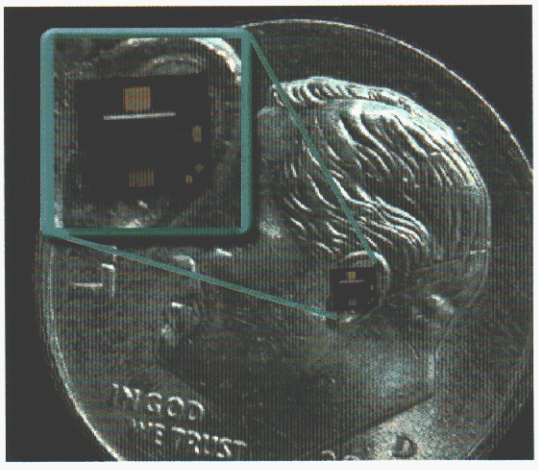

Figure 1. Picture of the 30 nl MEMS.

1.2. Equipment and Procedure

Sampling very small volumes necessitates the use of low outgassing materials, creative manifold design, and sensitive pressure measurements. All manifold components are made of stainless steel, and connections are either 1/16" compression or 1/4" metal gasket fittings. A schematic of the vacuum system and manifold is shown in Figure 2.

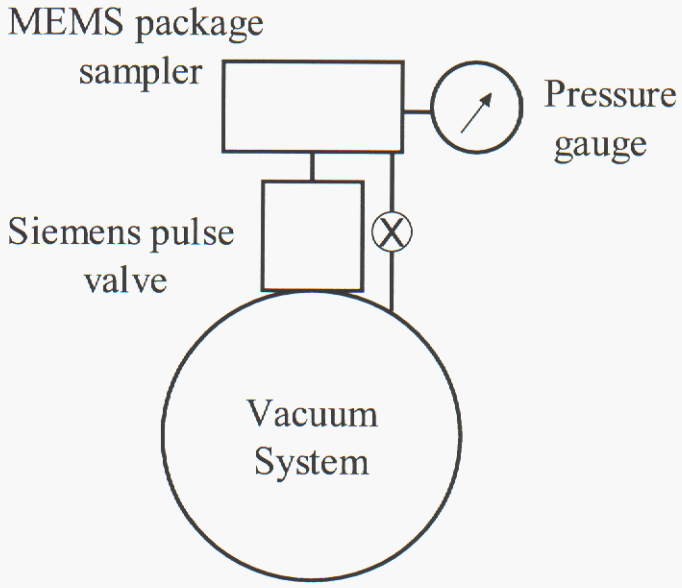

Figure 2. Schematic of gas sampling system for MEMS.

Manifold volumes are minimized to maximize the pressure obtained when gases within the packages are expanded into the manifold. The void volume within the MEMS package was measured dimensionally using a microscope and manifold volumes were measured using a variable volume (piston displacement) technique (5, 6).

Gas sampling involves manifold preparation, releasing the gases from the package, and analyzing the gases using a residual gas analyzer (RGA). The MEMS package is placed in the manifold, which is helium leak tested, and then evacuated overnight (base pressure: $<10^{-8}$ Torr). Baking is not necessary to achieve levels that are undetectable by the RGA. As with any hot filament instrument, the RGA has its own background (primarily CO, CO_2, H_2O, and H_2); however, the experimental method of measuring gas pulses makes correction for the constant background signals (discussed in the next section). After overnight evacuation, a second leak test is performed using both pressure rise and helium detection. During the pressure rise test, the manifold is isolated from the vacuum and the pressure gauge is monitored to make sure no detectable pressure rise is observed in 5 minutes. After passing all leak tests, the gases in the MEMS package are released by breaking the package in the "sampler" valve, a modified all-metal bellows valve (6LVV-MSM-DP-2-P). The resultant gas pressure in the manifold is measured with a modified Hastings solid-state pressure gauge (HPS-2002) calibrated with an MKS spinning rotor gauge (SRG-2CE). The manifold is equipped with a zirconium-seat pulse valve (Siemens Corp.) that introduces picoliter-sized gas pulses to the RGA (Stanford Research Systems, model 300). To increase mass spectral sensitivity, the vacuum for the RGA is

throttled using a manual valve to reduce the pumping efficiency and thereby increase the pressure of gas in the RGA manifold. Calibration curves for the RGA are generated by filling the manifold with pure gases and/or calibrated gas mixtures to approximately the same pressure as the sample pressure and measuring the peak heights from the gas pulses. A new set of calibration curves is generated on the same day that the MEMS package is sampled, without changing manifold configuration in any way (e.g., throttle valve setting). A sample calibration curve is presented in Figure 3 from which the RGA response as a function of pressure looks very linear.

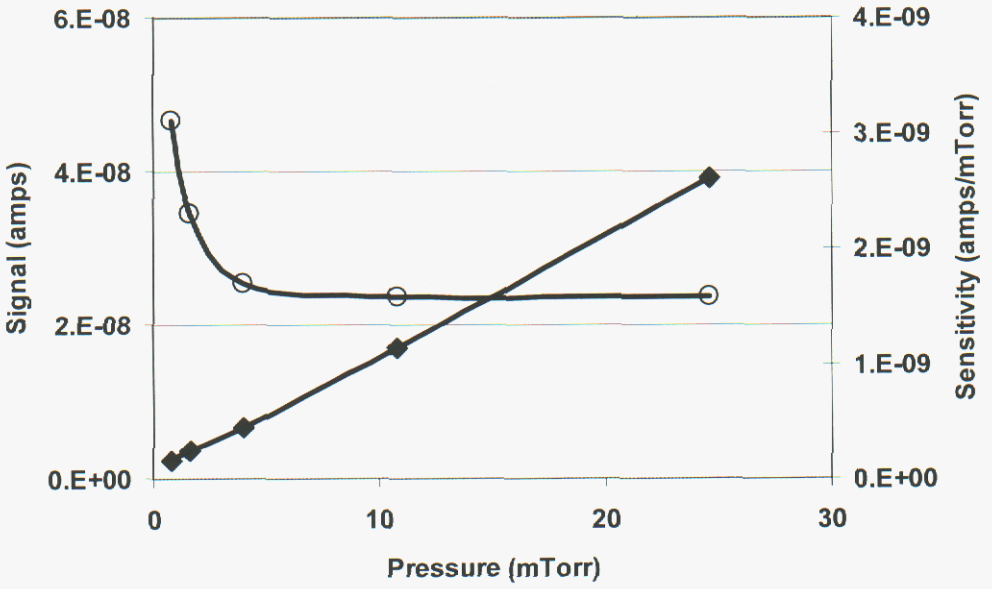

Figure 3. RGA linear response to nitrogen as a function of pressure (diamonds) and a plot of the calculated sensitivity as a function of pressure (circles).

The "sensitivity" of the RGA to a gas at a given pressure is calculated using the following equation.

$$S_i = \frac{H_i}{p_i} \tag{1}$$

where S_i is the sensitivity, H_i is the peak height, and p_i is the partial pressure for the i^{th} gas. However, when the sensitivity of the RGA output as a function of pressure is plotted, non-linearity is clearly observed. This nonlinearity observed is common and found at the extremes of the RGA's measurement range. Special care must be taken to account for the nonlinearity when making calculations. Clearly, an average sensitivity across the pressure range shown in Figure 3 would not provide maximum accuracy. In lieu of fitting the entire curve, sensitivity values were interpolated using the nearest pair of points encompassing the peak height for each gas from the MEMS sample. The differences in RGA response to different gases can be clearly seen in Figure 4 that shows the RGA response to various gases as a function of pressure.

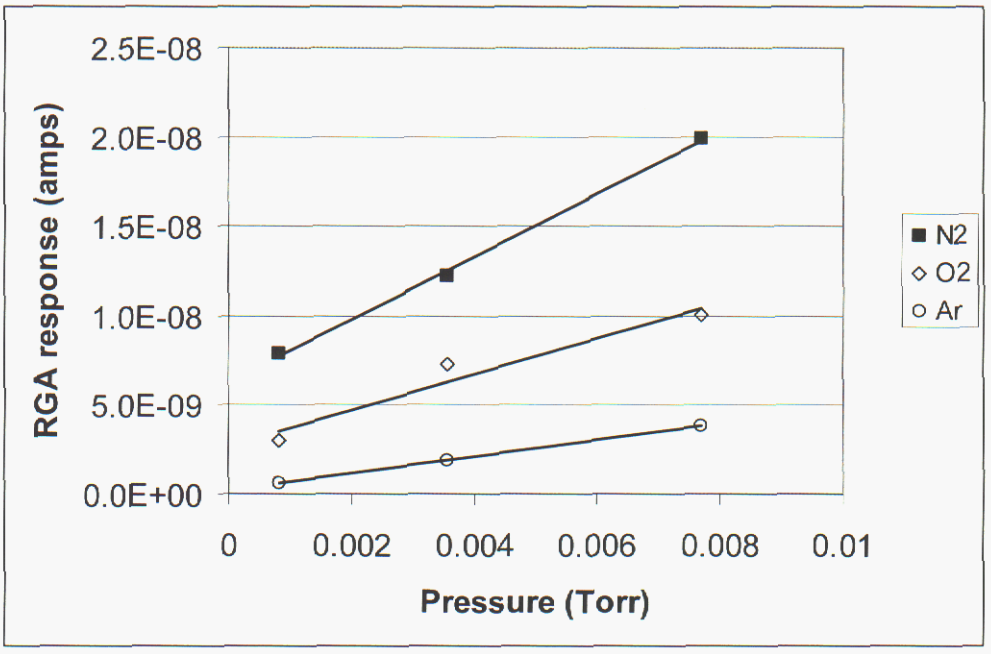

Figure 4. Sample calibration curve for the RGA response to various gas types and pressures.

1.3. Results

Several 30 nanoliter MEMS packages were gas sampled successfully and results showed the intended internal gas atmosphere of nitrogen was properly sealed inside most of the packages; however, significant oxygen was detected in some packages. A summary of the gas sampling results is shown in Table 1. Clearly, samples 1 and 2 are very hermetic and samples 3 and 4 are showing some air contribution. Upon further examination of the data (pressure stability) we cannot rule out the possibility of air leakage into the manifold for samples 3 and 4. Modifications to the manifold are underway to increase the robustness and to reduce the chance of leakage.

Table 1. Typical results obtained for 30 nl MEMS packages.

Sample	*Nitrogen*	*Oxygen*	*Argon*
1	99.6%	0.0%	0.4%
2	99.0%	0.0%	1.0%
3	95.2%	4.0%	0.7%
4	81.9%	17.3%	0.7%

As described previously, the gas analyses are performed by introducing gas pulses into the RGA. Typical data obtained from this measurement are shown in Figure 5. In the figure, four pulses of nitrogen gas from the manifold at a pressure of 3 x 10^{-3} Torr were

introduced into the RGA, which monitored the mass 28 (nitrogen and carbon monoxide) signal. The raw data are presented with no filtering or averaging, which shows a signal-to-noise ratio of approximately 10. The integrated signal (thick "stair-step" line in Figure 5a) and the plot of the step height (Figure 5b) show the consistent output obtained from the pulse valve and RGA. Integration reduces the inherent noise of the RGA while measuring small gas quantities.

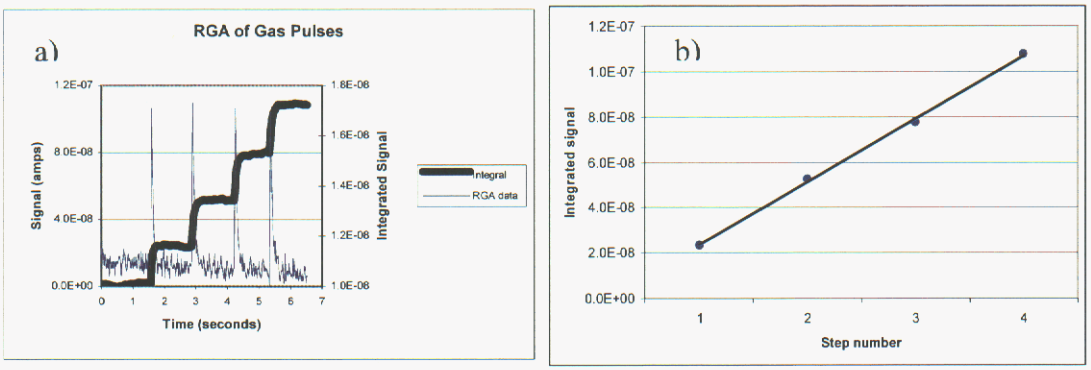

Figure 5. (a) Plot of four pulses of gas monitoring the mass 28 signal (nitrogen/carbon monoxide) in the RGA. (b) Plot of the four step heights from integral in the plot on the left demonstrating a high degree of linearity.

Several advantages are realized by using the picoliter pulse valve for sample introduction into the RGA. The first advantage is that the gas sample from the MEMS is conserved greatly by introducing only small aliquots into the mass spectrometer. This enables many analyses of the same sample over many minutes to hours, the only limitation being the magnitude of manifold outgassing and leakage. Second, a stable gas pressure pulse is presented to the RGA. Normally, gas is leaked into the RGA from a volume through a flow restrictor causing the gas pressure to decay as a function of time. This necessitates precise timing between standards and unknowns to ensure the measurements are taken on the same portion of the decay curve. However, with the pulse valve, such a small aliquot of gas is removed from the sample that the pressure reduction is negligible. Third, the multiple pulses provide a great opportunity to perform statistical analyses on the data. Due to the stable pulse heights, traditional statistics are easily applied to the data. Fourth, the sample size introduced into the RGA can be adjusted so the RGA signal can be optimized to maximize the signal (without going off scale) for various samples. MEMS packages come in many sizes and have a variety of internal pressures and gas types. Consequently, one rigid set of analytical conditions will not be optimum for all packages. Fifth, the pulses proved a unique way to correct for the RGA background by simply measuring the change (i.e., the pulse) above the constant background. Finally, the RGA background is kept low since the gas, which typically contributes significantly to the background through contamination, is introduced in such small quantities that the background isn't able to build up to detectable levels and the RGA stays very clean.

The ideal gas law is used to calculate the original gas pressure in the MEMS package before opening. The manifold volume was measured to be 7.5 cm^3 and the expanded pressure was typically around 3 x 10^{-3} Torr. By using the ideal gas law, the estimated internal gas pressure in the MEMS package is found by

$$P_1 = P_2 \cdot \frac{V_2}{V_1} \tag{2}$$

where P_1 is the internal pressure of the package, P_2 is the resultant pressure, V_1 is the volume of the package, and V_2 is the volume of the manifold as measured with the MEMS package in place in the manifold. The volume of the MEMS package is negligible with respect to the manifold volume so no correction is necessary to V_2; however, for larger packages, the correction can be significant so the term V_2 in Equation 2 becomes (V_1+V_2). By substituting values measured into Equation 2, the initial gas pressure inside the MEMS package is calculated to be

$$P_1 = (3 x 10^{-3}\ Torr) \cdot \frac{7.5\ cm^3}{30\ nl\ x 10^{-6}\ cm^3/nl} = 750\ Torr \tag{3}$$

Although this paper is focusing on the 30 nl packages, packages of various sizes have been analyzed using the pulse valve/RGA technique. Packages having internal gas volumes ranging from 30 nl to several hundred microliters have been successfully analyzed. The flexibility of the pulse valve makes possible these analyses by adjusting the amount of gas introduced into the RGA. Tests have shown the pulse valve to be able to easily control gas sample pressures ranging from sub-milliTorr to 1000 Torr. Thus, packages of virtually any size can be analyzed as long as the resultant gas sample pressures are in the stated range. Further tests are underway to determine the practical extremes for the gas analysis range; however, current tests are not at the limits of the pulse valve nor the RGA.

1.4. Conclusion

A technique for sampling extremely small MEMS packages was developed and successfully demonstrated. The technique is a radical jump from previous methods because not only were these MEMS packages sampled, but also the gas from each package was analyzed *dozens of times over the course of about 20 minutes*. Numerous improvements in the manifold (e.g., volume reduction, incorporation of solid state pressure sensor, novel crushing valve) enabled this sampling of 30 nl internal volume packages. This milestone in microanalyses makes possible the measurement of internal gas compositions of extremely small packages, which will enable better assessment of device hermeticity. Additionally, lessons learned from this work increase the fidelity of measurements made on larger packages by reducing outgassing, increasing RGA signals, and enabling multiple analyses for better statistics. Several parameters (e.g., pulse duration, RGA gain, vacuum throttle valve) can be adjusted to increase the signal-to-noise ratio even more.

2. ATTENUATED TOTAL REFLECTANCE STUDY OF FOTAS AND FOMAS IN MEMS ENVIRONMENT

2.1. Introduction

Our goal in this work is to use infrared (IR) spectroscopy to characterize vapor-phase-deposited self-assembled monolayers (VSAMs) in an environment similar to that in which they would be present in micro-electro-mechanical (MEMS) devices. Analysis of the vibrational modes present in the resulting IR spectra should reveal the chemical state of the VSAMs.

The absorption intensity achieved in single-pass transmission IR of monolayers is, however, typically too low to provide useful vibrational spectra. An IR technique that amplifies the absorption intensity is required.

Such amplification of the absorption intensity can be achieved by employing attenuated total reflection (ATR) spectroscopy. In this technique an IR beam is directed into thin ATR plate with beveled edges (generally a trapezoid or parallelepiped) at an angle that causes the beam to be totally internally reflected when it encounters the interface of the ATR plate with its external environment. The IR beam undergoes multiple such reflections as it traverses the ATR plate, and, at each reflection, an evanescent (non-propagating) IR wave penetrates a fraction of a wavelength into the external environment and interacts with materials on the surface of the ATR plate. If the material, say, a monolayer film, on the surface of the ATR plate absorbs IR, then each reflection approximates a single-pass transmission through it. The absorption intensity is multiplied by the number of reflections (often 50 – 100), and the resulting spectrum is in the form of one obtained by transmission rather than external reflection.

2.2. Experimental

IR spectroscopy using attenuated total reflectance has the sensitivity to provide good quality IR spectra from monolayers of films. For our purposes we require VSAMs to be present on a silicon surface, such as are present in MEMS devices, but ATR plates made of silicon absorb strongly in the IR fingerprint region and limit IR spectra to frequencies >1500 cm^{-1}. An ATR plate made of germanium allows access to frequencies as low as 800 cm^{-1}. To simulate a silicon/silicon oxide surface, we evaporated a thin (500 Å) film of silicon on a germanium ATR plate. The thin film of silicon provides a MEMS-like surface without limiting the IR bandpass of the germanium ATR plate. The germanium ATR plates are parallelepipeds 50 mm long by 10 mm wide by 1 mm thick. They were mounted in a commercial ATR accessory. Figure 6 shows a schematic diagram of the ATR/IR experiment.

Due to a small leak in the silicon deposition apparatus, the oxygen content was somewhat elevated in the silicon films on the germanium ATR plates. However, the elevated oxygen content provided surface silanol groups for expected reactions with VSAMs. We obtained single beam IR spectra of the germanium ATR plates both before and after

silicon deposition. The spectra obtained after silicon deposition were used as references to which the VSAM ATR spectra were ratioed, effectively compensating for any IR features (mainly Si-O) produced by absorption in the germanium plate or the silicon coating. A ThermoNicolet Nexus 870 Fourier transform infrared spectrometer was used to acquire the IR spectra.

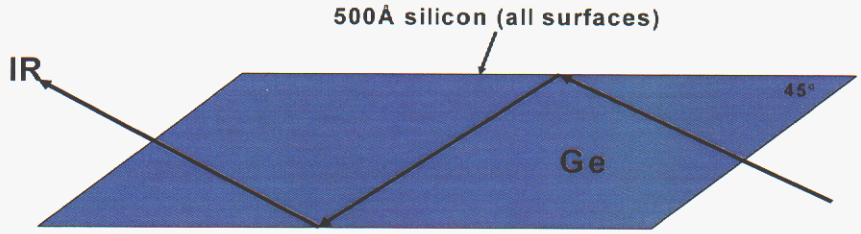

Figure 6. ATR-IR spectroscopy

Two materials FOTAS (perfluorooctyltris(dimethylamino)silane) and FOMAS (perfluorooctylmono(dimethylamino)dimethylsilane), see Figure 7, were evaporated as VSAMs on separate silicon-coated germanium ATR plates. IR spectra were obtained within ½ hour of removal from the evaporation apparatus and at intervals thereafter. We also obtained single-pass transmission spectra of FOTAS and FOMAS for comparison. To obtain the single-pass spectra, multi-micron-thick films of FOTAS and FOMAS were placed between salt (NaCl) windows and squeezed in a fixture that limited ingress of the ambient atmosphere, thereby slowing the interaction of the FOTAS and FOMAS films with air. The Si-N-$((CH_3)_2)_x$ groups (Figure 7) of FOTAS and FOMAS are especially labile with respect to reaction with ambient water vapor. Single-pass IR spectra of FOTAS and FOMAS were obtained within ½ hour (fresh) of placement between the salt windows and at intervals thereafter. The FOTAS film between salt windows was intentionally exposed to air and quickly gelled.

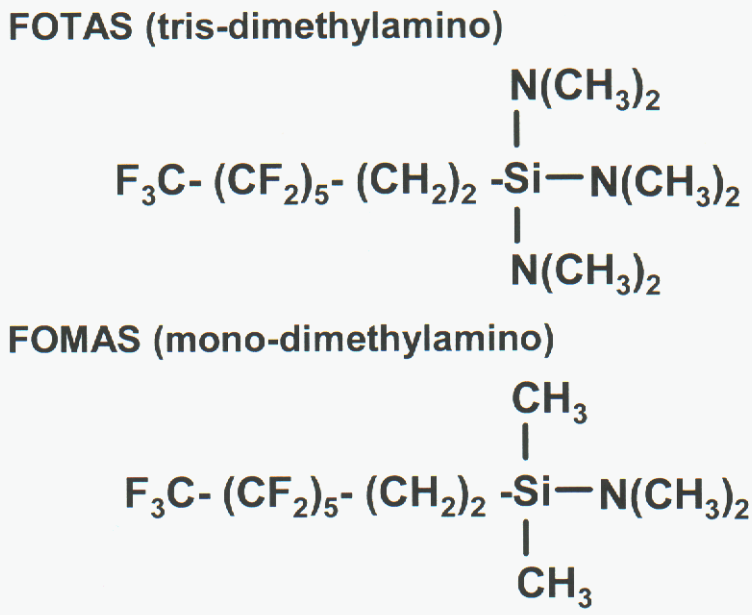

Figure 7. Chemical structure of FOTAS and FOMAS.

2.3. Results/Discussion

Single-pass transmission IR spectra of FOTAS between salt windows are shown in Figure 8. The spectrum of "fresh" FOTAS shows the expected bands in the "fingerprint" region of the IR spectrum. Bands due to the fluorocarbon tail (C-F) and the Si-N-$(CH_3)_2$ moieties are indicated in Figure 8. A spectrum of FOTAS obtained after two days between salt windows shows no significant differences from the spectrum of fresh FOTAS. After the FOTAS was exposed to air, there were significant differences in its spectrum. The C-F bands of the fluorocarbon tail remain, but the bands due to the Si-N-$(CH_3)_2$ groups have disappeared. In addition broad features have appeared in the region between 1000 and 1100 cm^{-1} and underlying the C-F bands in the 1100 to 1200 cm^{-1} region. These new bands are assigned to Si-O modes in Si-O-Si linkages, believed to be formed by the reaction of the dimethyl amine groups with ambient water vapor. A fairly complex assemblage of Si-O bands between 1000 and 1200 cm^{-1} occurs because there may be three Si-O-Si linkages in each FOTAS molecule. The C-H stretching region (2750 – 3000 cm^{-1}, not shown in Figure 8) of the IR spectrum of air-exposed FOTAS likewise shows loss of C-H modes in Si –N-$(CH_3)_2$ groups. Remaining C-H bands are due to the methylene groups attached to the fluorocarbon tail (Figure 7). The O-H stretching region (3000 – 3800 cm^{-1}) of the air-exposed FOTSA has a broad, low-intensity band possibly due to some Si-OH species, but most of the Si-O bonds are in Si-O-Si linkages.

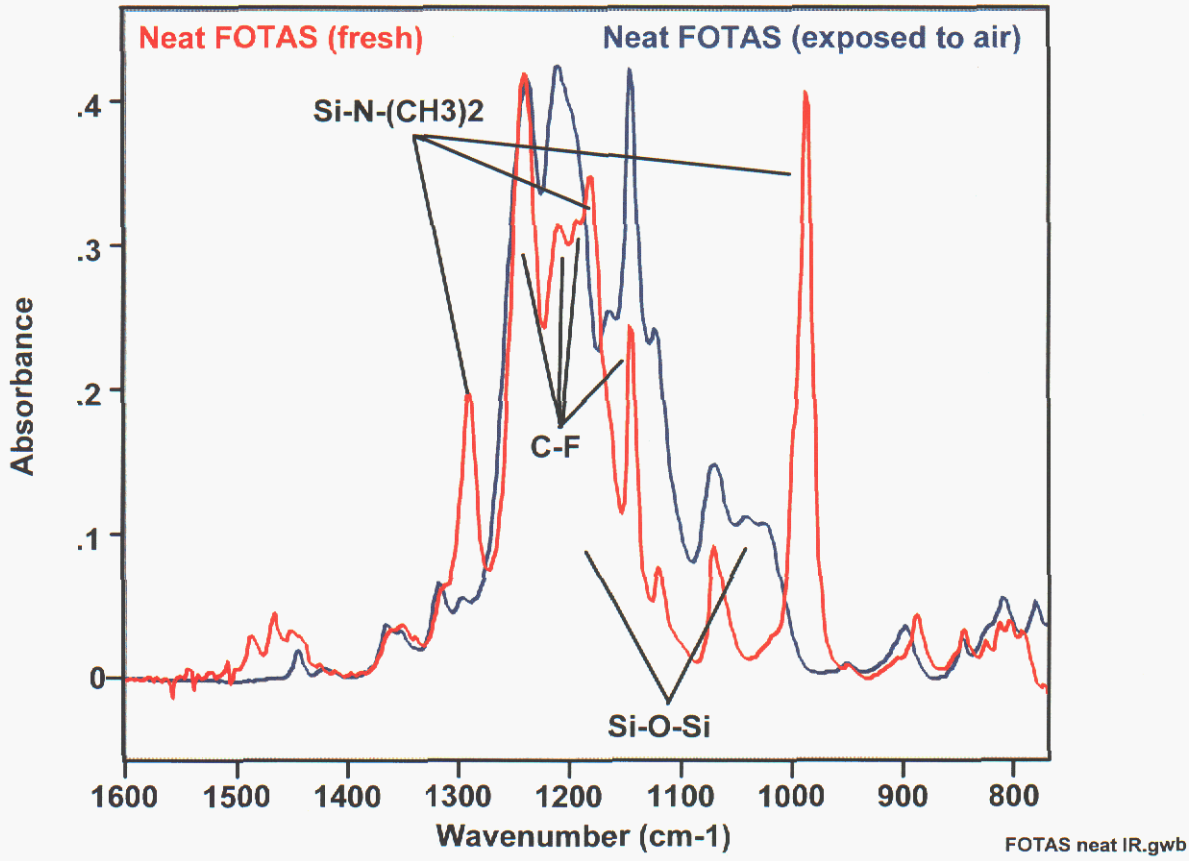

Figure 8. IR spectra of FOTAS (neat) between salt windows – freshly deposited and exposed to air.

Single-pass transmission IR spectra of FOMAS between salt windows are shown in Figure 9. The spectrum of "fresh" FOTAS shows the expected bands in the "fingerprint" region of the IR spectrum. Bands due to the fluorocarbon tail (C-F), the Si-N-$(CH_3)_2$ moieties and Si-CH_3 groups are indicated in Figure 9. Unlike the FOTAS film, which did not react significantly after two days without intentional exposure to air, the IR spectra of the FOMAS film between salt windows show that it has reacted in its holder after two days of aging. It is not known whether the FOMAS is more susceptible to reaction with ambient water vapor or whether the FOMAS holder was less effective in isolating the film from the ambient environment. After two days of aging, the spectrum of FOMAS shows retention of C-F bands from the fluorocarbon tail but, like reacted FOTAS, loss of bands due to Si –N-$(CH_3)_2$ groups. The intensity of bands due to Si –N-$(CH_3)_2$ groups is less in the fresh FOMAS spectrum (Figure 9) than in the fresh FOTAS spectrum (Figure 8) because FOTAS has three dimethyl amine groups to FOMAS' one. The presence of a (shifted due to reaction affecting the Si atom) band due to Si-CH_3 groups in the aged FOMAS spectrum indicates that Si-CH_3 groups have survived aging. The C-H stretching

region (2750 – 3000 cm^{-1}, not shown in Figure 9) of aged FOMAS also shows loss of C-H modes from Si –N-$(CH_3)_2$ groups but retention of C-H modes from Si-CH_3 groups. A single, relatively broad band due to Si-O-Si linkages appears in the aged FOMAS spectrum between 1000 and 1100 cm^{-1}. Reaction of the one dimethyl amine group in aged FOMAS leads to a single Si-O-Si linkage in the molecule and a simpler Si-O spectrum than reacted FOTAS. There is a relatively narrow band (not shown in Figure 9) near 3730 cm^{-1} in the spectrum of aged FOMAS that indicates the presence of some silanol (Si-OH) groups, but they are a minority compared to Si-O-Si linkages.

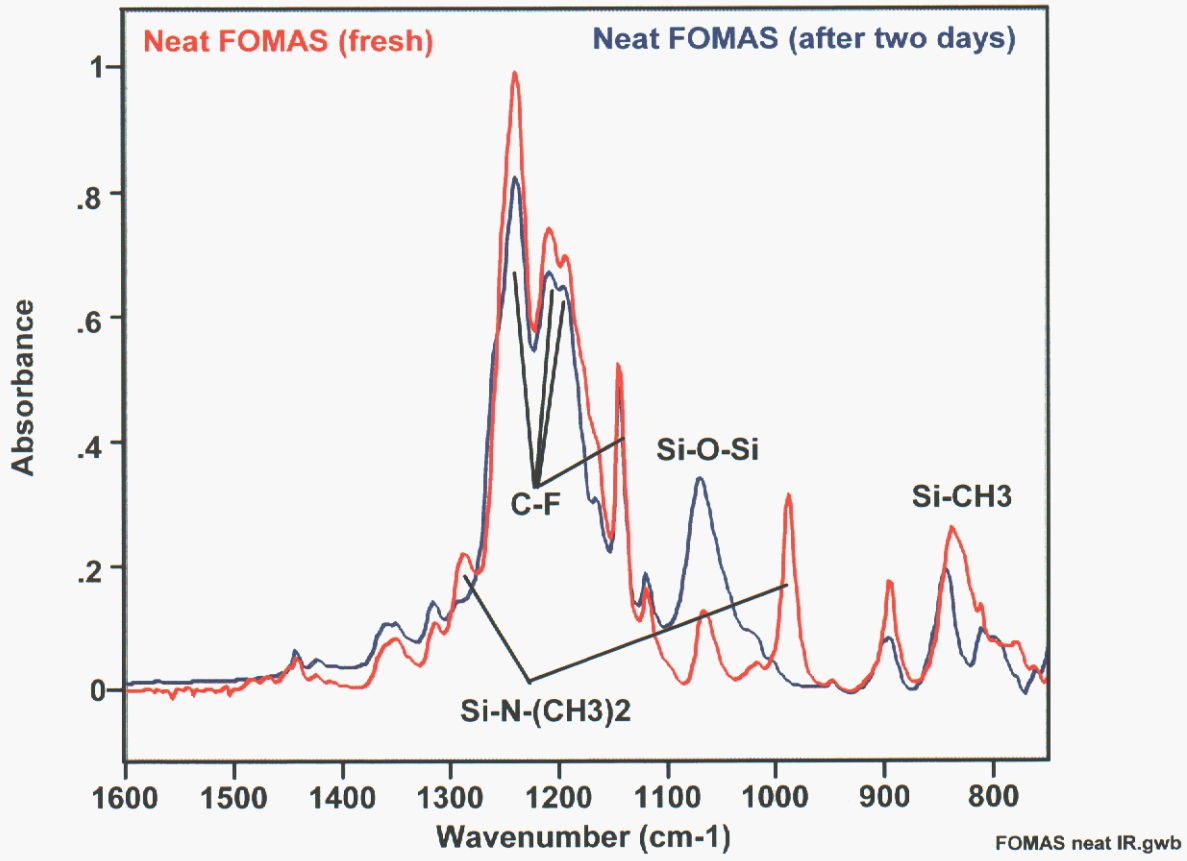

Figure 9. IR spectra of FOMAS (neat) between salt windows – freshly deposited and aged two days.

Figure 10 shows an ATR-IR spectrum of freshly-coated FOTAS on a Si-coated germanium ATR plate and the spectrum of fresh FOTAS between salt windows (compare Figure 8). C-F bands due to the fluorocarbon tail are retained in the ATR spectrum of FOTAS, but bands due to Si –N-$(CH_3)_2$ groups are not present. The ATR spectrum of FOTAS is dominated by a complex of broad bands from 1000 to 1200 cm^{-1} that we assign to Si-O-Si linkages. Note that orientation effects and proximity to the surface of the ATR plate can enhance the absorption intensity of portions of a molecule compared to others. In this case, we believe, the bands due to Si-O-Si linkages have been so enhanced. The FOTAS in the VSAM configuration on the ATR plate appears to have undergone complete reaction of its dimethyl amine groups to form Si-O-Si linkages. Additional

spectra of FOTAS on the Si-coated germanium ATR plate were acquired, over a four day period, with the FOTAS film exposed to ambient. No significant changes were noted in the ATR FOTAS spectrum.

In our ATR spectra, interpretation of C-H stretching region (2750 – 3000 cm^{-1}) has been complicated by the presence of hydrocarbon contaminants on the ATR plate prior to VSAM deposition (due to a delay between Si deposition and VSAM deposition). The hydrocarbons were removed by plasma cleaning prior to VSAM deposition, but their bands remained in the reference spectrum of the Si-coated Ge ATR plate to which all the subsequent spectra were ratioed. However, the O-H stretching region of the ATR FOTAS spectrum shows loss of some OH species and formation of others, suggesting reaction of silanols on the surface of the ATR plate with FOTAS and formation of different types of silanols, perhaps linked to FOTAS molecules. Again, Si-O-Si linkages outnumber silanol groups.

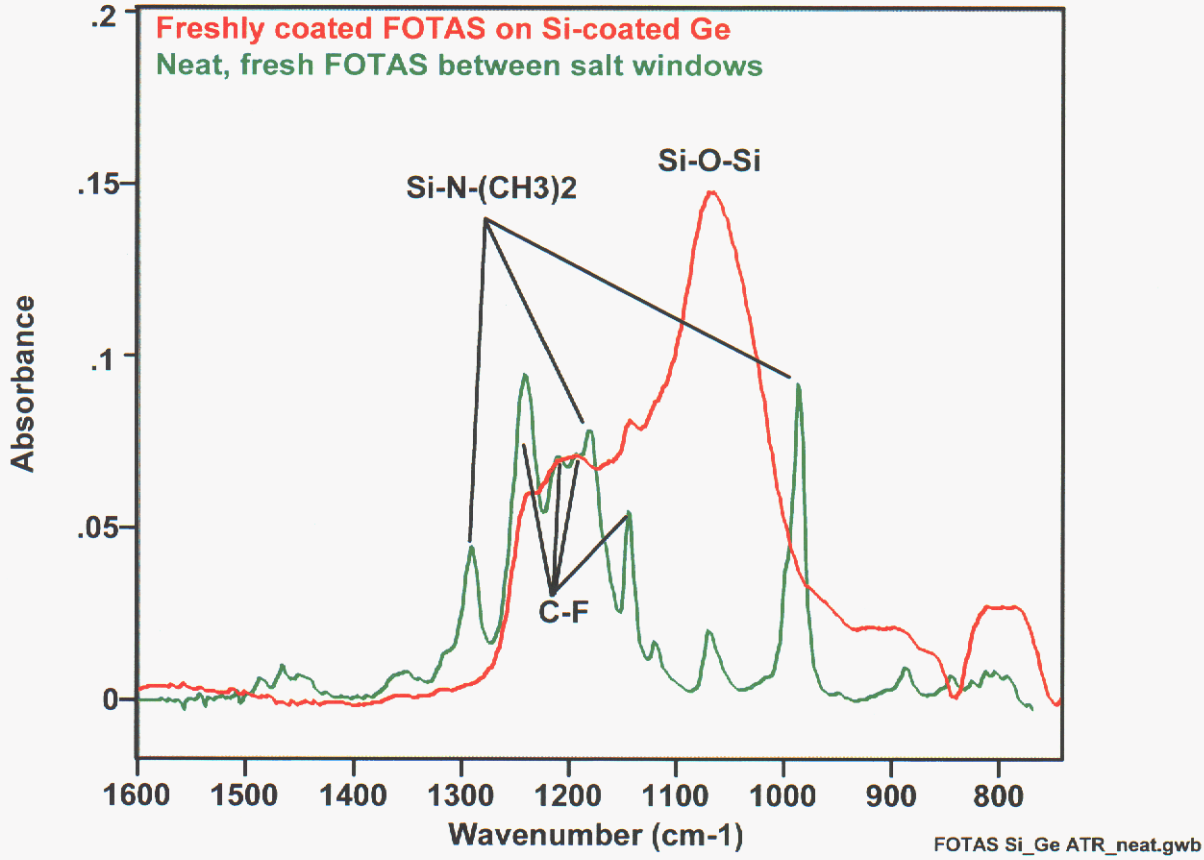

Figure 10. IR spectra of freshly-coated FOTAS on a Si-coated Ge ATR plate compared to neat, fresh FOTAS between salt windows.

Figure 11 shows an ATR-IR spectrum of freshly-coated FOMAS on a Si-coated germanium ATR plate and the spectrum of fresh FOMAS between salt windows (compare Figure 9). C-F bands due to the fluorocarbon tail are retained in the ATR spectrum of FOTAS, but bands due to Si –N-$(CH_3)_2$ groups are not present. Compared to

the FOTAS ATR spectrum (Figure 10), the C-F bands in the FOMAS ATR spectrum are more prominent, and there is less intensity in the portion of the Si-O-Si band complex between 1100 and 1200 cm^{-1}. As we noted earlier, this difference in band patterns is consistent with a maximum of one Si-O-Si linkage in FOMAS (as a result of dimethyl amine reaction) versus three in FOTAS, with the result that the Si-O-Si band intensity in the reacted FOMAS spectra is more concentrated between 1000 and 1100 cm^{-1}. The retention of a Si-C band in the ATR spectrum of freshly deposited FOMAS indicates that, at least initially, its Si-CH_3 groups are still present and that only the dimethyl amine group has reacted.

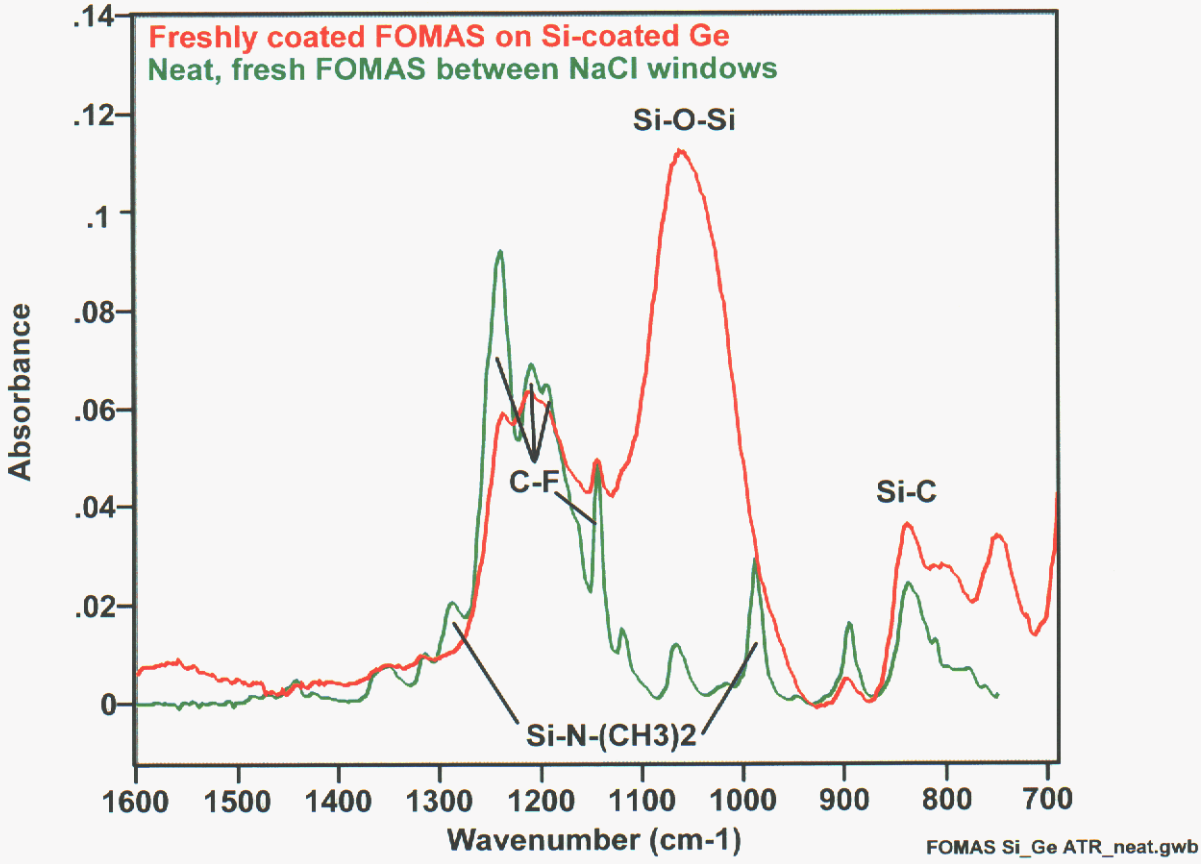

Figure 11. IR spectra of freshly-coated FOMAS on a Si-coated Ge ATR plate compared to neat, fresh FOMAS between salt windows.

Unlike the ATR spectrum of FOTAS, the ATR spectrum of FOMAS changes significantly with ambient aging (Figure 12). ATR spectra of freshly deposited (within a half an hour) FOMAS on a Si-coated germanium plate taken a few minutes apart show no significant difference, but detectable changes occur in the FOMAS spectrum after two hours of aging, and the trends become readily apparent after four days of ambient exposure. These trends include loss of intensity in bands assigned to Si-C modes and an increase in Si-O-Si band intensity, especially in the 1100 – 1200 cm^{-1} region. As shown in Figure 13, The ATR spectrum of FOMAS, with ambient aging, comes to look more like that of FOTAS.

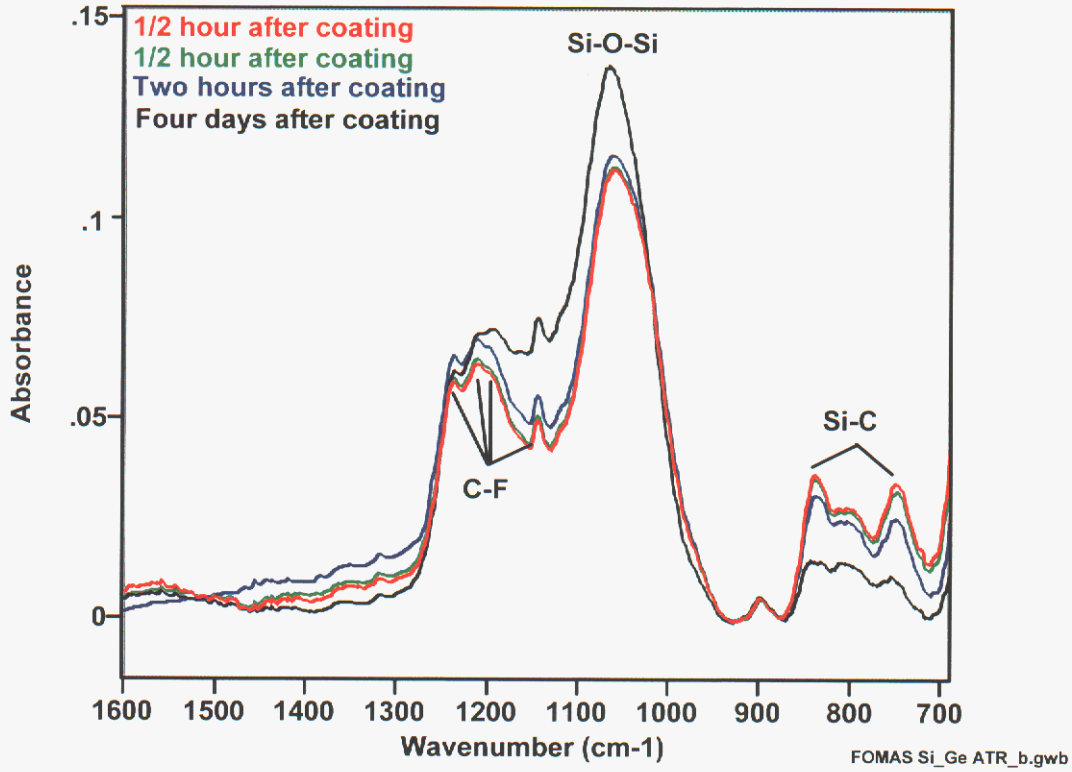

Figure 12. IR spectra of freshly-coated and aged FOMAS on a Si-coated Ge ATR plate.

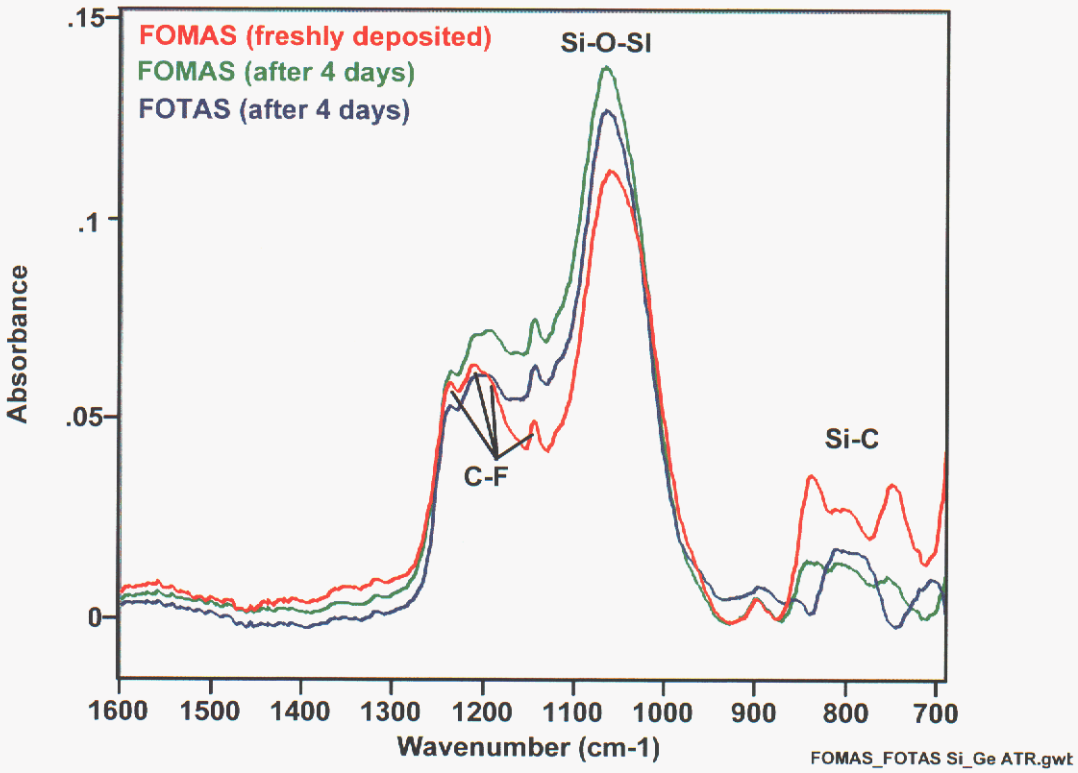

Figure 13. Comparison of IR spectra of FOMAS and FOTAS on a Si-coated Ge ATR plate.

FOTAS and FOMAS, as multi-micron-thick films between salt windows, initially yield single-pass IR spectra characteristic of their molecules in an unreacted state. Eventual exposure to ambient atmosphere results in hydrolysis of the dimethyl amine groups to form Si-O-Si linkages. Silanol groups may also be formed by the reaction, but they are in the minority. The IR spectra are consistent with complete hydrolysis of dimethyl amine groups, resulting in multiple Si-O-Si linkages per FOTAS molecule and a single Si-O-Si linkage per FOMAS molecule. The $Si-CH_3$ bonds in FOMAS show no evidence of reaction when in a multi-micron film between salt windows. ATR-IR spectra of FOTAS, in a VSAM deposition on a Si-coated germanium plate and exposed to ambient, show that it reacts the same way as in a multi-micron-thick film. Reaction of its dimethyl amine groups appears to be prompt and complete, forming multiple Si-O-Si linkages per FOTAS molecule. The ATR-IR spectra of a FOTAS VSAM deposition, aged for four days, show no evidence of significant change in the structure of the molecule with aging. ATR-IR spectra of FOMAS, in a VSAM deposition on a Si-coated germanium plate and exposed to ambient, show that it also undergoes prompt and complete hydrolysis of its lone dimethyl amine, with a simpler Si-O-Si structure. However, on aging in ambient, the FOMAS VSAM deposition undergoes further reaction, which, as indicated by ATR-IR spectra, involves loss of $Si-CH_3$ bonds and formation of additional Si-O-Si linkages. At this point the aged FOMAS VSAM and the FOTAS VSAM should be chemically very similar, with their silicon atoms bonded to three oxygen atoms and to the same ethylene/fluorocarbon tail. The ATR-IR spectra of aged FOTAS and FOMAS reflect this similarity.

2.4. Conclusion

There is no immediately apparent explanation for the difference in reactivity of the $Si-CH_3$ groups in VSAM-deposited FOMAS versus FOMAS in a multi-micron film between salt windows. However, these experiments do show the ability of ATR-IR to reveal the structure of VSAM-deposited molecules in a MEMS-like environment. We recommend a repetition of these experiments to include continued aging of the VSAM films.

3. SECTION 3: A STRATEGY FOR CHARACTERIZING SAM FILMS IN MEMS DEVICES

3.1. Introduction

Molecular level films have become the preferred way of tailoring the surface properties in microelectromechanical systems (MEMS). The primary motivation for surface modification is the need to control stiction or electrostatic binding between opposing Si surfaces during both the chemical release of the device (release stiction) or during device use (in-use stiction). Additional concerns arise when considering the need to control the tribological properties (i.e. coefficients of static and dynamic friction) of contacting surfaces, like gear-and-hub regions. The state-of-the-art approach to minimizing inter-surface forces is to lower the energy of these surfaces using self-assembled monolayers (SAMs). Sandia National Laboratories uses a vapor-deposited SAM (VSAM) molecule (FOTAS or (1H,1H,2H,2H-perfluorooctyl)tris(dimethylamino)silane) to minimize surface energy (7). The presence of this molecule on the various MEMS device surfaces can be used as a chemical marker with which to access the state-of-health of the surface.

Degradative mechanisms potentially active during device lifetime could be expected to alter the SAM film. As a result, chemical and structural changes in the SAM film become signals of the initiation or propagation of aging related processes that might alter device reliability. The approach used in this part of the project was to first characterize the SAM film and learn how to quantify the state of the film. Select general degradative mechanisms were then proposed and experiments were designed to identify whether changes in the film characteristics could be determined using the analytical techniques available. Finally, the suite of analytical methods developed and demonstrated in this project was applied to packaged MEMS devices.

The degradative mechanisms of interest addressed in this project involve processes that result in significant modification of the SAM film and its properties. Three general processes of interest are 1) the displacement of FOTAS molecules, 2) contaminant adsorption onto and incorporation into the FOTAS film, and 3) penetration of surface active species like H_2O to the FOTAS/device interface. Figure 14 shows a summary of these mechanisms, a schematic representation of the impact on film structure, and a proposed experiment that would produce a chemical signature most like the degradative process. For example, an investigation of how time-of-flight secondary ion mass spectrometric (TOF-SIMS) relative ion yields vary as a function of surface coverage of FOTAS (θ_{FOTAS}) provides a chemical signature for local SAM displacement using the same characterization technique. Specific mechanisms, like H_2O penetration through the FOTAS film, may be more readily probed by conducting direct aging experiments. A directed aging experiment addresses the question of what the consequences are of a specific processes taking place as opposed to what are the chemical and physical constituents necessary to drive a specific mechanism, the latter representing the traditional accelerated aging experiment.

The focus of this part of the project is the FOTAS – Si system. This emphasis is given because of Sandia's investment in FOTAS as the preferred VSAM for MEMS applications. The techniques described in this section and the knowledge gained in this work are applicable to other molecular film materials systems.

3.2. XPS-based Quantification of SAM Surface Concentrations

X-ray induced photoelectron emission can be used to identify the presence of the fluorocarbon-based SAM species on a silicon surface. Figure 14 shows a series of C(1s) spectra acquired as a function of varying exposure to FOTAS.

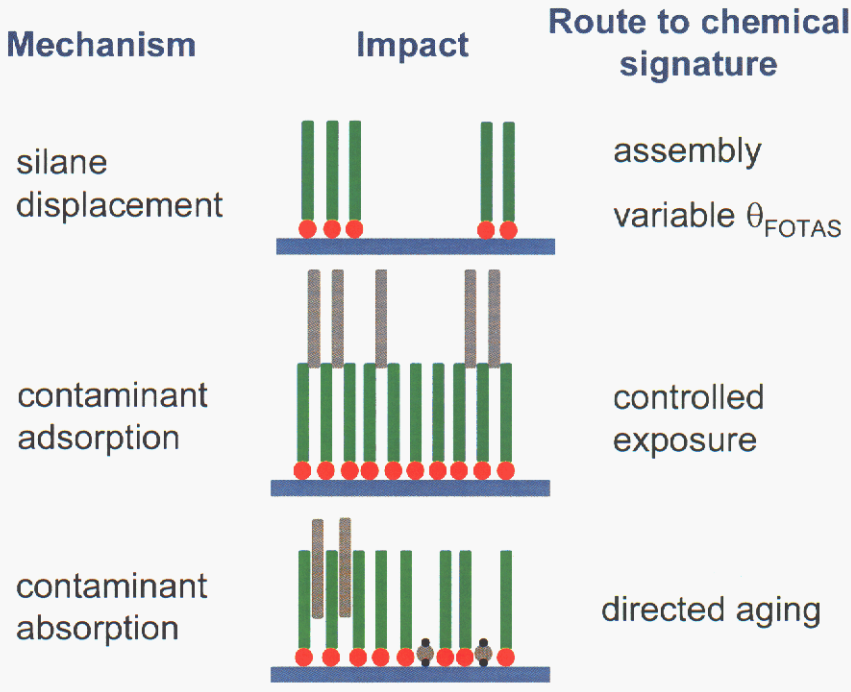

Figure 14. Proposed mechanisms and schematic impact of SAM degradation on a Si substrate. Approaches for determining what signatures might accompany these mechanisms are also given.

A monochromatic Al(Kα) source was used to minimize x-ray and electron degradation of the monolayer film. Spectra generated at low exposure levels show a series of closely spaced peaks in binding energy at 284.6, 286.3 and 288.6 eV. These features correspond to emission of methylene carbon (-CH_2-), ether carbon (-CH_2-O-), and carbonyl carbon (-C=O) atoms, respectively, and simply reflect the extent of oxidation of the emitting carbon atom. Increased exposure produces attenuation in these intensities and the appearance and growth of two well resolved peaks at higher binding energy. Peaks observed at 290.9 and 293.3 eV correspond to emission from fluoromethylene carbon (-CF_2-) and the trifluoromethyl carbon (-CF_3), respectively. In addition, increased FOTAS exposure produces the retention of intensity in a broad, unresolved feature centered on 284.9 eV. This latter feature is consistent with emission from the methylene carbon atoms

that link the fluorinated pendant chain to the active Si head group of the molecule. These two carbons are denoted as being located at the α and β positions of the molecular structure shown in Figure 15.

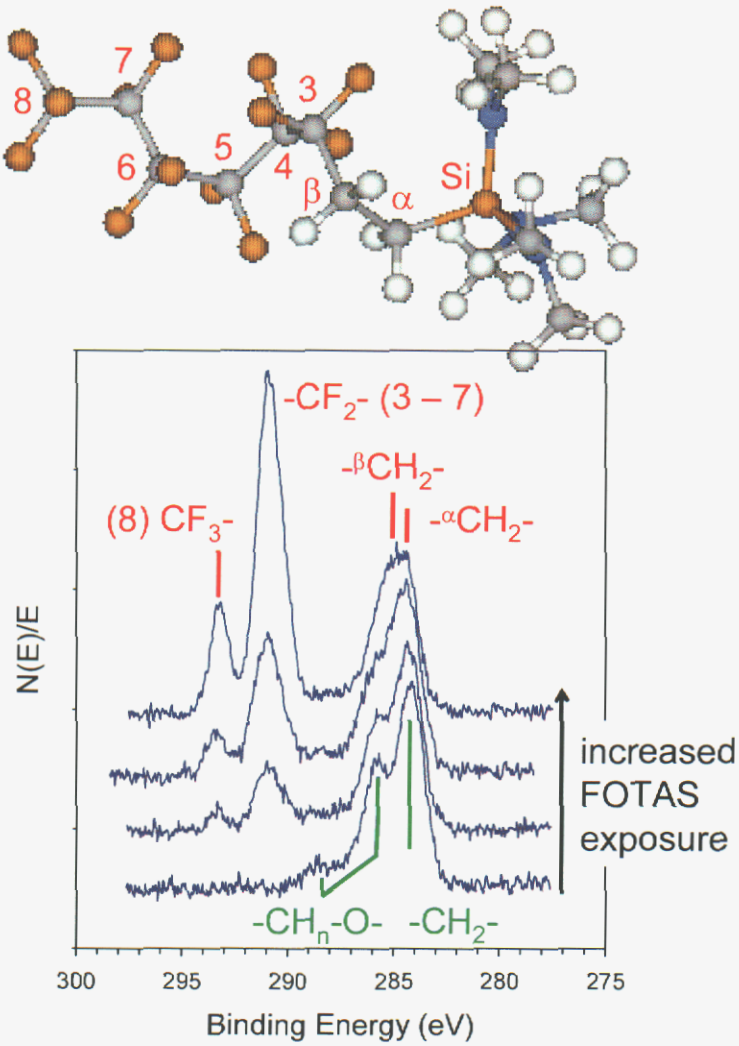

Figure 15. Variation in the monochromatic Al(Kα) induced C(1s) lineshape as a function of increased exposure of a polycrystalline Si surface to FOTAS.

The $^{\beta}CH_2$ center would be expected to be more electropositive than aliphatic CH_2 due to its proximity to the fluorinated pendant chain through an inductive effect. But, this carbon center would not be as electropositive as an ether-like carbon positioning its emission peak intermediate between those observed for the initial hydrocarbon contaminant observed on the surface. The $^{\alpha}CH_2$ center appears comparable in charge state to an aliphatic methylene carbon and overlaps in position with the dominant hydrocarbon contaminant peak observed at low FOTAS coverage.

The three dimthylamino ligands bound to the Si head group are cleaved at some stage in the vapor phase reaction and this species is lost from the surface. XPS analysis shows no evidence of N(1s) emission which should be present at the surface concentrations probed in this study given the signal-to-noise achieved in these measurements. Much more sensitive TOF-SIMS analysis (> 10X sensitivity improvement over XPS) yields no indication of N-containing secondary ion fragments. Presumably, these ligands are hydrolytically cleaved at various stages during or even after deposition of the molecule to form volatile dimethylamine. Remnant surface H_2O, possibly interacting with silanol (Si-OH) surface moieties and generated during the H_2 containing O_2 plasma cleaning process, is most likely responsible for this nucleophilic substitution reaction. Dimethylamino ligands retained after deposition would be expected to react with atmospheric moisture after removal from the deposition system.

The data displayed in Figure 15 can be used to quantify the surface FOTAS coverage. Specifically, the quantity of interest is the number of FOTAS molecules per unit area or areal density. One approach to determining this value is to compute the ratio of the C atomic concentration in the SAM film to the Si atomic concentration in first plane of Si atoms in the underlying oxide. This approach requires treating the amorphous oxide as a crystalline analog to approximate the location of the individual cation and anion sublattices. A tridymite structure is assumed for this reason (8). The corresponding expression relating XPS integrated intensities to concentration is given by:

$$\frac{I_C}{I_{Si}^s} = \frac{N_C}{N_{Si}} \cdot \frac{\sigma_C}{\sigma_{Si}} \cdot \frac{L_C}{L_{Si}} \cdot \frac{T_C}{T_C} \cdot \frac{f_C}{f_{Si}} \qquad (4)$$

The I terms represent integrated intensities from the photoemission spectra with the I^s superscript denoting that it only includes the fractional intensity from the outermost layer of Si. The N terms are the atomic concentration of C in the SAM film and Si in the outermost layer expressed in units of atoms·cm^{-2}. N_C is what is being solved for and N_{Si} is taken to be 9.1×10^{14} cm^{-2} following the assumption of a tridymite structure. σ, L and T are the photoemission cross sections (9), the angular asymmetry for emission from s and p orbitals (10), and a net transmission function for the analyzer used.[1] The factor f takes into account photoelectron scattering due to the presence of the FOTAS molecule. For the outermost plane of Si atoms, f_{Si} is an attenuation factor that is FOTAS coverage (θ) dependent:

$$f_{Si} = 1 - \theta[1 - \exp(-d^{SAM} / \lambda_{Si}^{SAM}) \qquad (5)$$

where d^{SAM} is the thickness of the FOTAS monolayer, which is assumed in this case to be equivalent to the length of the pendant chain oriented perpendicular to the surface plane and λ_{Si}^{SAM} is the attenuation length of Si photoelectrons in the SAM phase. The f_C factor takes into account a higher probability of C(1s) photoelectron scattering in the SAM pendant chain for electrons emitted from methylene and fluoromethylene closer to the substrate surface.

[1] Information supplied by Kratos for the UltraAxis system.

The remaining material system parameters for these equations are determined using a variety of techniques combined with published values in the literature. I^{S}_{Si} is figured by integrating the scattering function using a spectroscopic ellipsomteric determined value of 1.5 nm for the SiO_2 oxide thickness and an $\lambda_{Si}^{SiO_2}$ value (attenuation length of the Si(2p) photoelectron in SiO_2) value of 3.4 nm determined by angle resolved XPS in the absence of a FOTAS film. The resulting integral represents the total intensity for the $Si^{4+}(2p_{3/2,/1/2})$ expected for the full oxide. The outer layer fraction of this intensity is computed by ratioing the Si sublattice length by the total thickness of the oxide. λ^{SAM} at the kinetic energies of C(1s) and Si(2p) emission can be estimated to be 3.9 and 4.4 nm, respectively, from Tougaard's measurements of a comparably sized alkylthiol on Au (11). d^{SAM} is calculated to be 1.2 nm assuming the chain is sufficiently short to assume a zig-zag tetrahedral conformation. It is noted that the fluorocarbon chain could assume a helical conformation producing a small discrepancy in the assumed pendant chain length (12). Finally, θ is calculated based on contact angle measurements with H_2O, immediately.

$$\cos\phi = \theta_{SAM}\cos\phi_{SAM} + (1-\theta_{SAM})\cos\phi_{SiO2} \qquad (6)$$

after samples are removed form the deposition chamber, using the Cassie equation (13):

In this equation, the contact angles ϕ are the values measured in this study for a saturated FOTAS monolayer or 117° and a clean SiO_2 control surface or 0°.

One remaining factor that is taken into account in these measurements is degradation due to x-ray exposure. FOTAS intensity loss and residual hydrocarbon increases are observed in the 20 minute period required to generate spectra like those shown in Figure 15. The intensities used to compute N_C are corrected for these small but measurable changes.

Solving equation 4 for the C areal density and accounting for 8 carbon atoms per FOTAS molecule results in a variation in the molecular density with deposition time as shown in Figure 16.

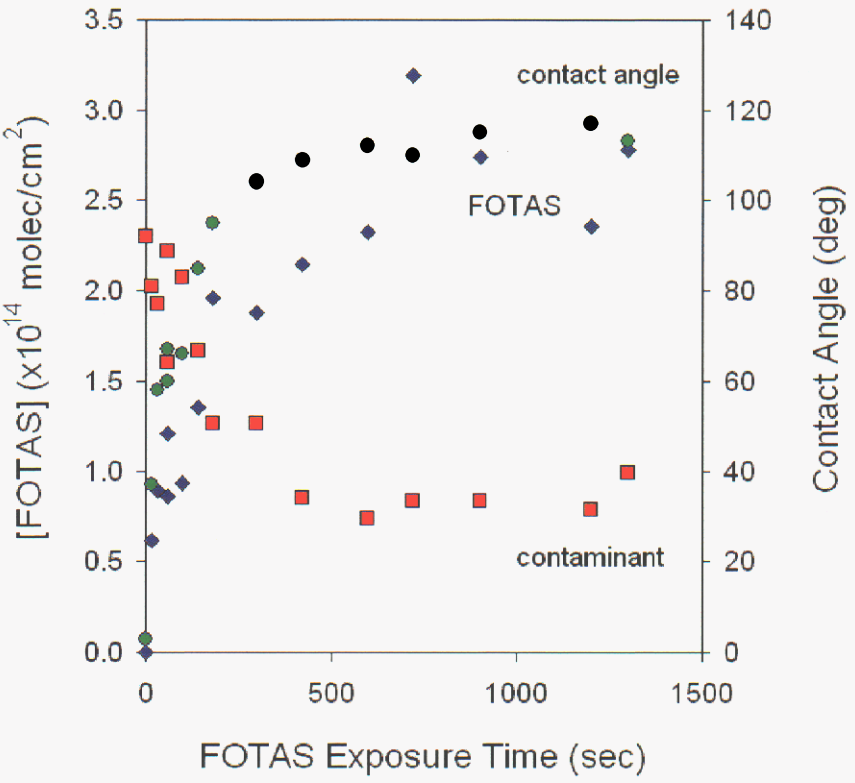

Figure 16. Variation in the surface concentration of FOTAS (◊) and the measured contact angle (•) as a function of deposition time on polycrystalline Si. The residual, contaminant hydrocarbon concentration (■) is also included where molecular density is derived.

The curve shows a rapid uptake of FOTAS on the surface over the first 3 minutes of exposure with eventual saturation at a molecular density of 2.8×10^{14} molec·cm^{-2}. An accurate measurement of FOTAS partial pressure is not made during this deposition and, as a result, an adsorption probability (or sticking coefficient) of the molecule on the surface cannot be calculated. The significance of this saturation value is that it is equivalent to the QCM determined value of 2.8×10^{14} molec·cm^{-2} measured by Mayer et. al. using microgravimetry for the trichlorosilane analog of this molecule (14). Langmuir films of fluoroalkanes and fluoroalkylthiols typically exhibit molecular areas consistent with a density of 3.4×10^{14} molec·cm^{-2} (15) indicating that the resulting FOTAS film on SiO_2 does not exhibit the tight packing of a liquid compressed fluoroalkane film. In addition, the molecular density is also considerably lower than the estimated surface silanol concentration of 4.6×10^{14} OH moeities·cm^{-2} indicating that potential siloxane surface bridge sites are not fully utilized (16). Given the arguments presented by Stevens (8) concerning shorter chain molecular binding and interchain cross-linking, these molecules are spaced to far apart to form cross-linking bonds between the Si head groups or they form clusters with some degree of cross-linking and open regions available for subsequent adsorption of contaminant species.

This less than optimum packing density of the FOTAS molecules allows for the adsorption of contaminant hydrocarbon species within the film. Fitting of XPS spectra based on the stoichiometry of the FOTAS pendant chain results in residual C(1s)

integrated intensity. This residual intensity is also plotted in Figure 15 and shows a continuous decline with increased FOTAS concentration. TOF-SIMS measurements made on these samples indicate that the chemical form of this contaminant is principally short chain (3 and 4 carbon) molecules one or two oxygen atoms, such as simple aldehydes, ketones, esters or carboxylic acids. The source of this contaminant is presumably through atmospheric exposure after surface processing and FOTAS deposition. Given the SIMS determined molecular size, the contaminant accounts for approximately 20% of the total molecular content of a saturated FOTAS film.

Several key lessons result from these surface characterization experiments. Monochromatic XPS is demonstrated as a quantitative tool for determining the SAM surface concentration on MEMS device-level substrates. Under ideal conditions, the device-level surface is expected to contain approximately two thirds of the ideal packing density of a fluoroalkane surface phase (15). As much as 20% of molecular content of the surface is made up of short chain hydrocarbon contaminants. It is this surface description that might undergo changes as the surface is modified through MEMS module packaging, use, and aging.

3.3. TOF-SIMS Characterization of SAM Films

These quantitative XPS results can be used to calibrate TOF-SIMS analysis of the FOTAS/Si system. Calibration is required because secondary ion emission is an inherently difficult phenomenon to quantify. Material specific models and molecular dynamics simulations of the collision cascade induced by an incident primary ion and the impact of this cascade on secondary ion production and escape from the surface are only in their infancy. Despite this limitation, the SIMS experiment contains a large quantity of information and is ideally suited for MEMS structures. Calibration of SIMS data follows two different paths in this project: 1) a simple univariate approach and 2) a multivariate method utilizing Sandia's copywritten AXSIA approach. The univariate approach is discussed below and is applied in a number of the following sections. The multivariate approach is discussed in several papers appended to this LDRD project report.

A univariate calibration method is based on evaluating how select secondary ion intensities vary with known FOTAS surface coverage. Ions of interest are those that can be related to the parent FOTAS molecule based on anticipated fragmentation paths. A representative secondary ion mass spectrum for a FOTAS saturated polycrystalline Si surface is shown in Figure 17.

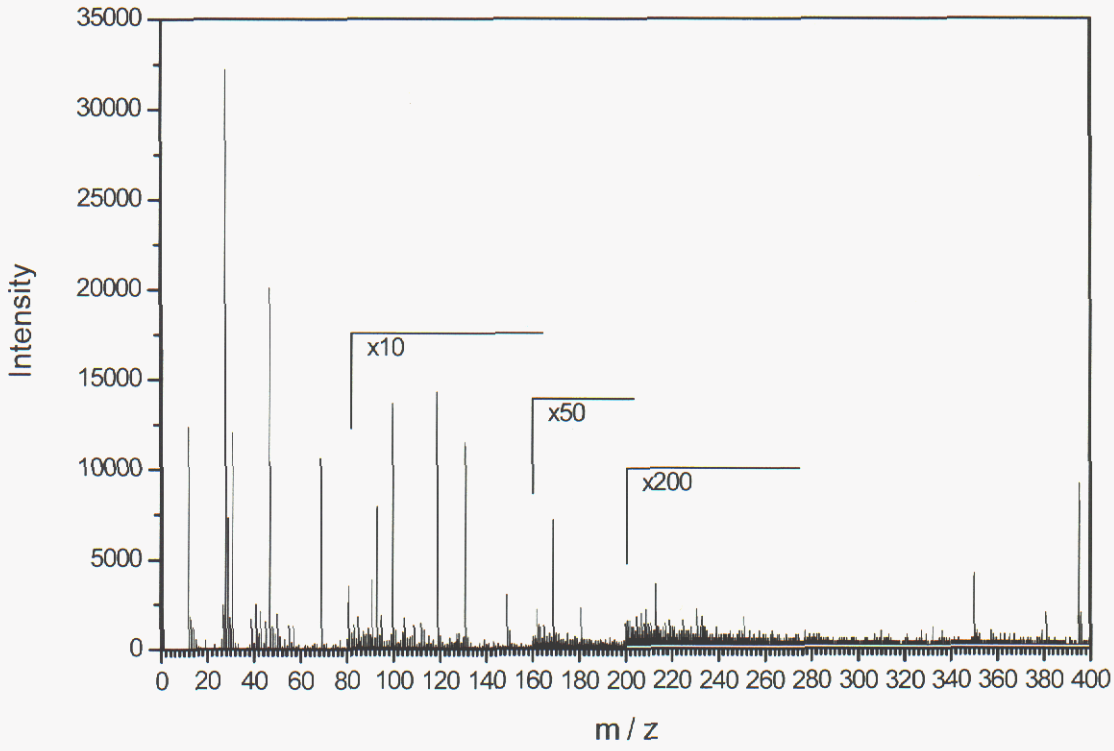

Figure 17. Typical ToF-SIMS spectrum of a FOTAS saturated polycrystalline Si surface using a 25 keV $^{69}Ga^{+}$ source. Select portions of the spectrum are magnified in ion intensity (i.e. x10) to highlight the higher mass range.

A list of detected positive ions that are observed in our analysis with a 25 keV $^{69}Ga^{+}$ source is shown in Table 2 with the origin of the ion included.

Table 2. Positive ions expected for and observed in SIMS measurements using a 25 keV $^{69}Ga^{+}$ incident ion. Mass-to-charge ratio (m/z) values are given in units of Dalton (D).

m/z	Species	Origin	m/z	Species	Origin
1.008	H	Contaminant+FOTAS	65.974	SiF_2	Substrate+FOTAS
12.000	C	Contaminant+FOTAS	67.055	C_5H_7	Contaminant
13.008	CH	Contaminant+FOTAS	68.995	CF_3	FOTAS
14.016	CH_2	Contaminant+FOTAS	73.997	C_3F_2	FOTAS
15.024	CH_3	Contaminant+FOTAS	75.007	SiC_2H_4F	FOTAS
18.998	F	FOTAS	80.995	C_2F_3	FOTAS
26.016	C_2H_2	Contaminant+FOTAS	81.070	C_6H_9	Contaminant
27.024	C_2H_3	Contaminant+FOTAS	84.972	SiF_3	Substrate+FOTAS
27.977	Si	Substrate+FOTAS	91.055	C_7H_7	Phthalate
28.977	^{29}Si	Substrate+FOTAS	92.995	C_3F_3	FOTAS
29.974	^{30}Si	Substrate+FOTAS	95.011	$C_3H_2F_3$	FOTAS
30.998	CF	FOTAS	99.994	C_2F_4	FOTAS
32.006	CHF	FOTAS	104.026	C_7H_4O	Phthalate
33.014	CH_2F	FOTAS	105.034	C_7H_5O	Phthalate
39.024	C_3H_3	Contaminant+FOTAS	109.027	$C_4H_4F_3$	FOTAS
41.039	C_3H_5	Contaminant+FOTAS	111.994	C_3F_4	FOTAS
43.055	C_3H_7	Contaminant+FOTAS	115.055	C_9H_7	Contaminant
44.980	SiOH	Substrate	118.992	C_2F_5	FOTAS
46.975	SiF	Substrate+FOTAS	123.994	C_4F_4	FOTAS
47.975	^{29}SiF	Substrate+FOTAS	130.992	C_3F_5	FOTAS
48.972	^{30}SiF	Substrate+FOTAS	149.024	$C_8H_5O_3$	Phthalate
49.997	CF_2	FOTAS	161.990	C_4F_6	FOTAS
53.039	C_4H_5	Contaminant	168.989	C_3F_7	FOTAS
54.998	C_3F	FOTAS	180.991	$SiC_3H_3F_6$	FOTAS
55.018	C_3H_3O	Contaminant	230.986	C_5F_9	FOTAS
55.055	C_4H_7	Contaminant	251.048	$C_6H_8F_9$	FOTAS
57.070	C_4H_9	Contaminant	262.992	C_6HF_{10}	FOTAS
59.032	SiC_2H_7	FOTAS	350.000	???	FOTAS?
61.997	C_2F_2	FOTAS	381.978	$SiC_7H_3F_{14}$	FOTAS
64.012	$C_2H_2F_2$	FOTAS	394.994	$SiC_8H_5F_{14}$	FOTAS

Figure 18 shows a plot of the relative intensity of these ions as a function of XPS-derived surface concentration of FOTAS.

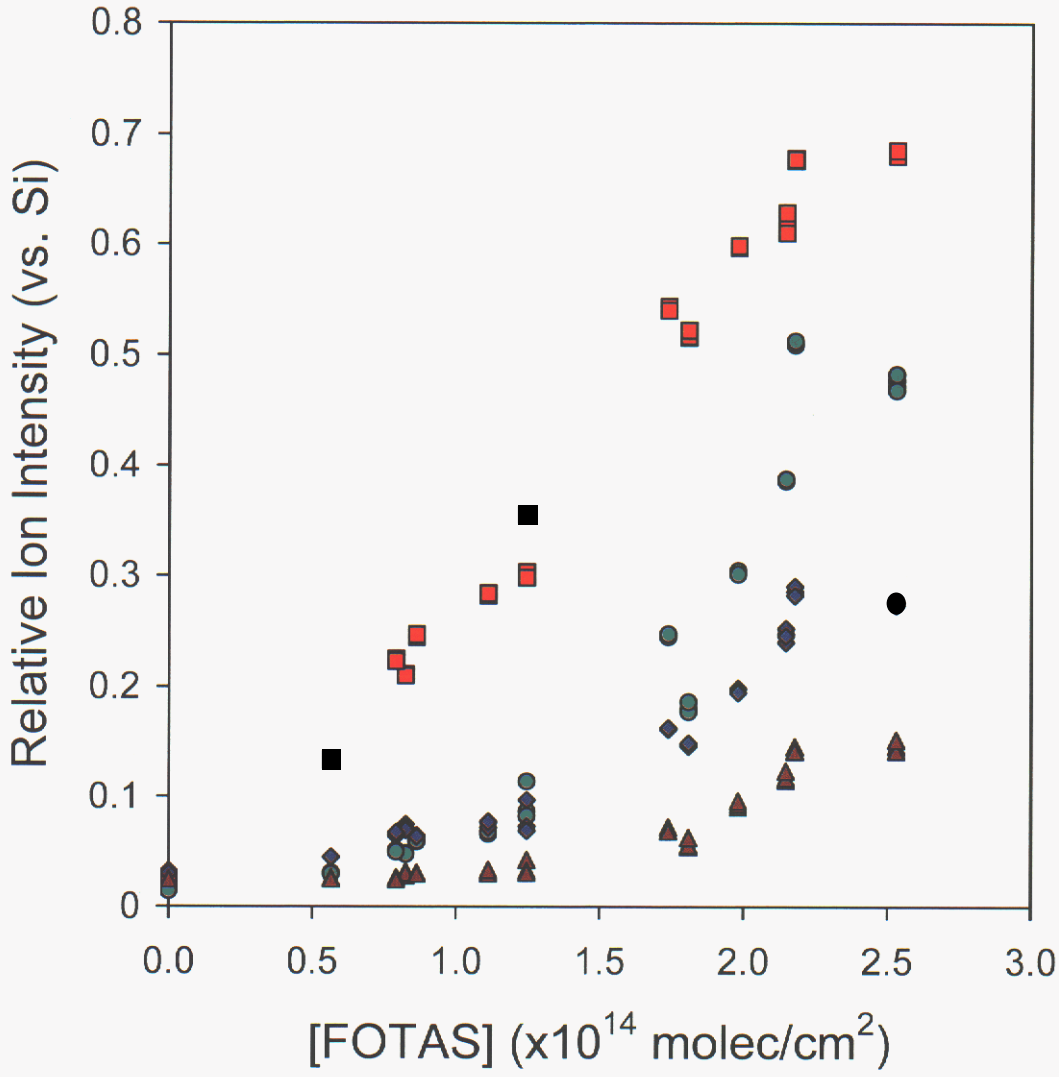

Figure 18. Variation in relative SIMS positive ion intensity as a function of XPS-derived FOTAS surface concentration for polycrystalline Si: SiF^+ (■), CF_3CF_2 (●), $CF_3(CF_2)_2$ (♦), and $CF_3CF_2(CF)_2$ (▲).

The ion intensities are normalized to that of Si^+ to minimize instrumental variance during the course of this analysis. Low mass ions, like SiF^+, CF^+ and CF_3^+, are the most intense as expected for the high fragmentation efficiency exhibited by the 25 keV Ga^+ source used. The relative intensities scale in a continuous fashion with the FOTAS concentration. Higher mass ions characteristic of the perfluorinated pendant chain are also detected with reasonable a signal-to-noise ratio and also exhibit increased relative intensity with increased SAM concentration. Calibration is based on establishing a functional relationship between an ion of interest and the FOTAS concentration. This univariate method has been used to quantify silane concentrations on MEMS modules where limited available area precludes the possibility of an XPS measurement.

3.4. Quantitation at the Device Level

The XPS and SIMS techniques can be combined to quantify SAM surface coverage at the device level. As part of the outreach of this project, personnel have been characterizing MEMS modules for several concurrent projects as a way of validating the technique development and knowledge gained. An example of this effort is shown in Figure 19 where a test module designed by M. Dugger (1824) was analyzed using SIMS.

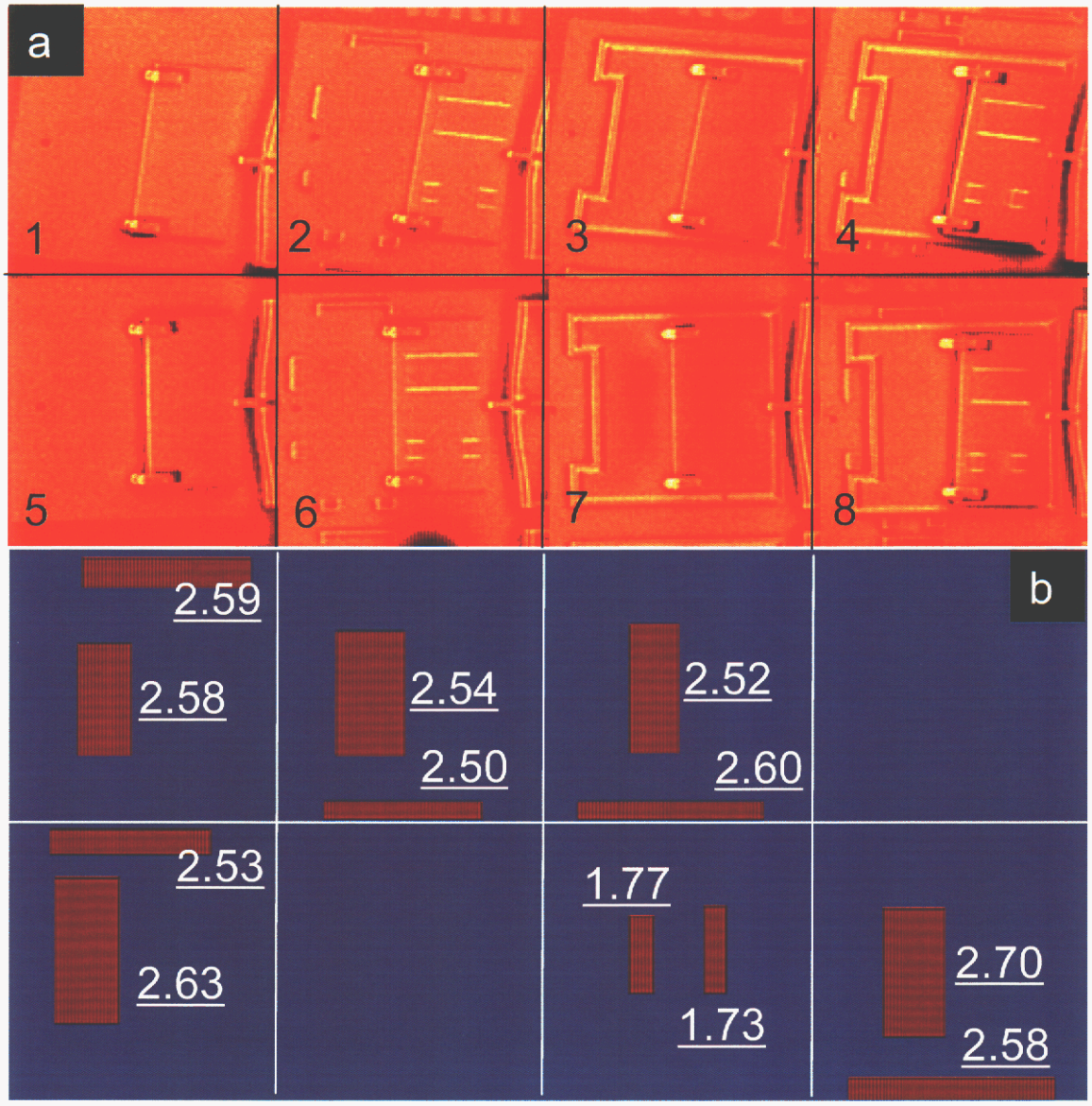

Figure 19. SIMS cumulative ion image (a) of 8 select devices (grid lines mark perimeter of analyzed region) on a MEMS test module and a schematic image (b) showing regions of quantification (red rectangles). Horizontally elongated regions are line-of-sight areas while vertically elongated regions are occluded areas during the VSAM deposition. Underlined numbers are FOTAS molecular concentrations ($x10^{14}$ molec·cm^{-2}) and demonstrate the ability of FOTAS to quantitatively fill occluded surface area at the device level (MEMS modules courtesy of M. Dugger, SNL, 1824).

This specific module included a series of Si flaps latched and hinged to the surface during the deposition of FOTAS. These flaps are unlatched and flipped prior to analysis to determine how effectively cleaning reagents from the plasma and the silane precursor can transport through minimum conductance channels to effectively coat occluded surfaces. These surfaces simulate worst case conditions (to some limit) for vital internal surfaces associated with pin joints and gear hubs that currently do not show improved operation performance with the deposition of the VSAM.

A set of cumulative ion images are shown in Figure 19a for a set of eight of these flap structures. The variation in pixel intensity is a result of variable secondary ion emission over the full 300 D mass range analyzed. Large variation in intensity is observed at the perimeters of structure fabricated in the Si that are primarily the result of accentuated electric field facilitating ion escape from the surface. A more subtle variation in intensity is visible when comparing the line-of-sight perimeter regions of the devices (near the grid lines in the images) with the occluded surfaces in the center of the device images. Of particular note are the low intensity areas underneath the exposed flap for device 7. This specific device exhibited a strongly adhering flap to the underlying surface and considerable force was required to flip it over. The schematic shown in Figure 19b contains a series of red rectangular regions where quantitation has been applied by correlating SiF^+/Si^+ ratios with XPS-derived surface concentrations. The underlined numbers in this schematic indicate the local surface concentration in units of 10^{14} moelcules·cm^{-2}. With the exception of device 7, the FOTAS concentrations are quite comparable independent of whether a surface has line-of-sight access to the VSAM deposition environment. Given a typical sacrificial oxide layer thickness of 2 μm, these 100 x 50 μm flap structures possess considerable conductance limitations to vapor-phase mass transport. The concentration values suggest that surface cleaning and FOTAS deposition are quite efficient processes. The cumulative secondary ion intensity variations are created by more subtle effects. There is a limitation to this efficiency as evidenced by the low concentration found for the occluded regions of device 7.

This correlated SIMS/XPS data demonstrates that it is possible to quantify molecular layer concentrations at the device level. This accomplishment was one of the key objectives of this project.

3.5. AFM Detection of FOTAS Films

Atomic Force Microscopy is one of the higher spatial resolution techniques available for surface characterization. Resolution is limited by the tip radius, with 1 nm tips commercially available, the magnitude of the tip – surface force field being detected, a combination of how this field propagates through space and how it is sensed (field or field gradient), and lastly by the surface topography. The latter parameter serves to spatially convolute force fields greatly diminishing resolution. MEMS device–level substrates are polycrystalline and topographically rough producing a unique set of challenges for detecting the presence of the FOTAS film.

Imaging of the SAM film is possible by exploiting large force fields at large tip – surface distances that minimize the effects of surface roughness. One approach to this type of imaging is to exploit long range electrostatic force with a Kelvin force probe. In this experiment, a conductive AFM tip is scanned a known distance from the sample surface and the potential required to minimize the electrostatic force sensed by the tip is measured. Successful imaging requires that the FOTAS molecules contribute to the creation of an electrostatic field and that this field varies in some predictable fashion with the FOTAS molecule surface concentration.

Perfluoroalkylsilane pendant chains are expected to possess significant dipole moments. The bound molecule can be viewed as an electropositive Si head group (bound to a SiO_2 surface) with an electronegative (electron withdrawing) fluoroalkyl terminal group. This view establishes the existence of charge separation and essentially its direction in space, the two key components for a molecular dipole. More attention has been given to computing dipole moments of perfluoroalkylthiols in consideration of SAM film formation on Au surfaces. Quantum mechanical calculations show values -1 to -2 D (1 D or Debye = 3.33×10^{-30} C·m) are typical for these molecules with a dipole orientation that systematically oscillates with the number of fluoromethylene groups in the pendant chain.

The consequence of the presence of a surface dipole is that it should result in a net increase or decrease in surface potential depending on sign. Based on the previous discussion, surface potential should be an indicator of the presence of the type of molecule and its average concentration and orientation. The concept of presence and type in the fluoroalkylsilane/Si system is readily demonstrated by examining lithographically patterned silanes on Si. Figure 20 shows surface potential maps for octadecyltrichlorosilane (ODTS) and (1H,1H,2H,2H-perfluorodecyl)trichlorosilane (FDTS) on Si(100).

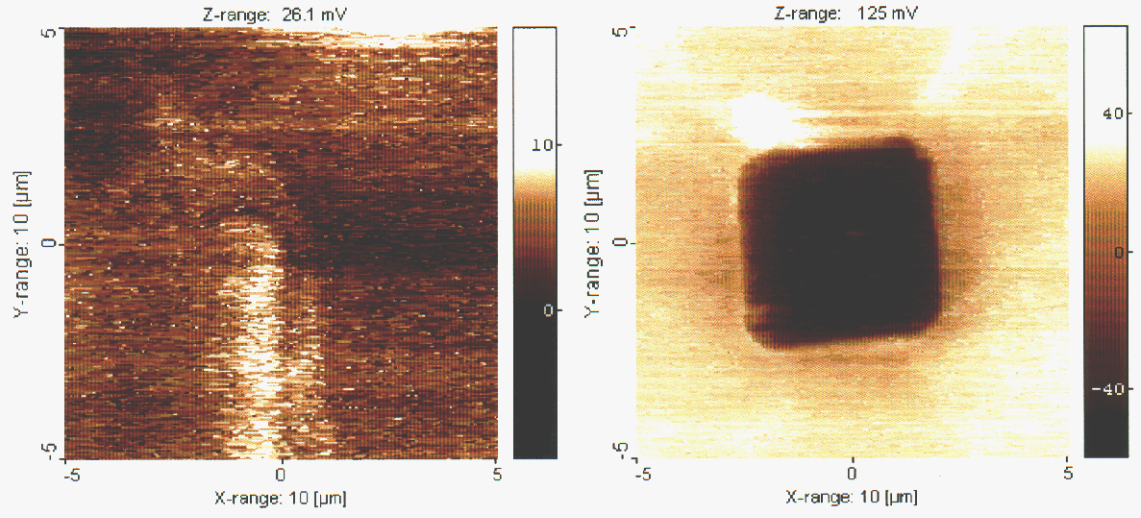

Figure 20. Surface potential images generated from SKFM of lithographically patterned silane islands on Si(100): a) a 50x50 µm^2 ODTS island and b) a 5x5 µm^2 FDTS island. The ODTS island occupies the lower left quadrant of the image in a).

The images were acquired in an amplitude modulation mode using a commercially available cantilever (Pt coated, f_o = 60 kHz, < 20 nm tip radius) scanned 30 nm above the surface. A corner of a 50 x 50 μm^2 non-fluorinated ODTS domain is imaged in Figure 20a. A small positive potential of +20 mV is measured for the ODTS region relative to the surrounding Si substrate. The 5 x 5 μm^2 fluorinated FDTS domain imaged in Figure 20b shows a -127 mV potential decrease when compared to the surrounding Si substrate. The measurements are complicated by the fact that the chemical composition of both the silane island and the surrounding Si is not known to any quantitative extent (i.e. surface concentration of ODTS and FDTS) and the potential is expected to be modified by contaminant incorporation and adsorption in either domain. We may assume that short-chain hydrocarbons occupy these regions much like the non-saturated FOTAS/Si surfaces discussed in the XPS and SIMS analysis sections. The longer chain protonated silane would be expected to have a slightly more positive dipole relative to the shorter chain hydrocarbons (17), so the potential would increase as observed. The perfluorinated silane should produce a much larger potential decrease because of the larger expected negative dipole (17). These images demonstrate the fact that both presence and type of molecule can be inferred from these types of relative surface potential measurements.

The potential of SAM coated Si surface can also be tracked as a function of SAM coverage. Figure 21 shows the results of this type of measurement for FOTAS on polycrystalline Si as a function of the XPS determined surface concentration.

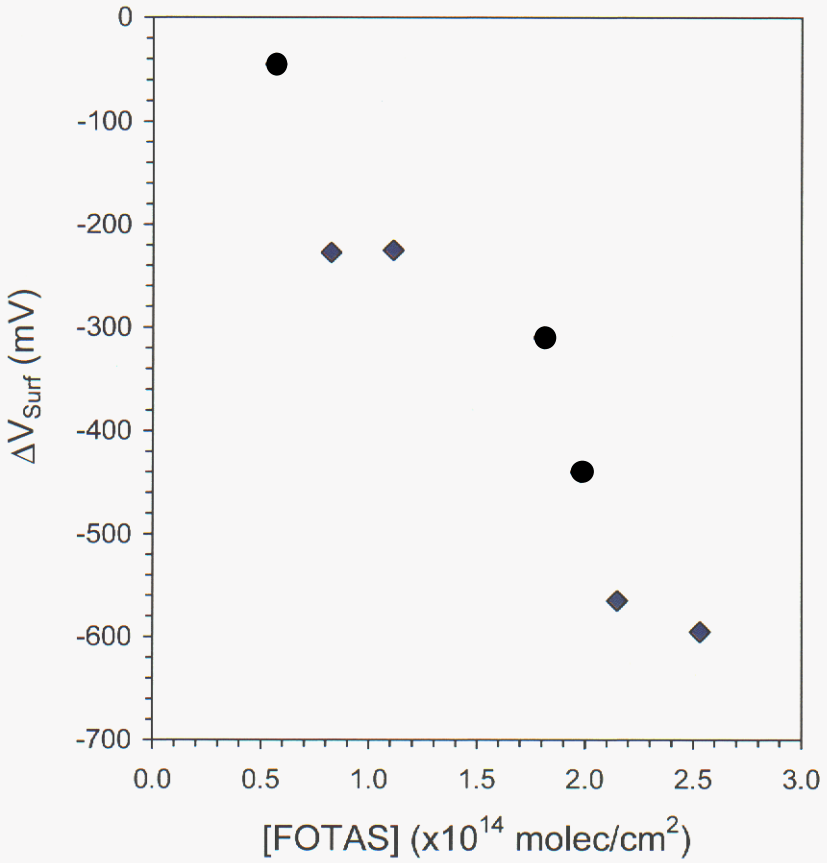

Figure 21. Variation in the surface potential for polycrystalline Si as a function of FOTAS coverage.

This data shows a monotonic decrease in the surface potential with increasing surface coverage. Using the formalism of Howell et al. (18), we anticipate a linear variation of surface potential (V_S) with SAM concentration according to:

$$V_S = \frac{[FOTAS] \cdot (\vec{p} \cdot \hat{n})}{2K\varepsilon_o}$$

where p·n represents the dot product of the molecular dipole moment and a unit vector normal to the surface, K the dielectric constant of monolayer, and ε_o is the permittivity of free space. The near linearity of the data of Figure 21 suggests that FOTAS molecules assume an essentially fixed orientation that is independent of concentration to within the accuracy of a linear description of the data. Assuming a normal orientation to the surface and a K of 2, a dipole moment of -2.5 D is computed for FOTAS. This value compares favorably to computed values of -2.38D for a perfluorodecyltrimethoxysilane on Si (17) and -1.9 D measured for C_{16} perfluoroalkanes on Au (19). We note that in the former case only -225 mV surface potential differences were measured using SKFM relative to the vacuum ultraviolet patterned and oxidized Si substrate. The larger values measured for the FOTAS films discussed in this report may be the result of higher packing densities, more vertical orientation of the dipole axis, and fewer contaminants. No additional characterization was reported for the perfluorodecyltrimethoxysilane films and these films were deposited in air at elevated temperatures, so film composition is uncertain.

The SKFM technique is capable of detecting small spatial variations in the FOTAS concentration on device-level Si. An example is show in Figure 22 where the topographic and surface potential images are shown for a polycrystalline Si surface with a FOTAS concentration of $8x10^{13}$ molec·cm^{-2}.

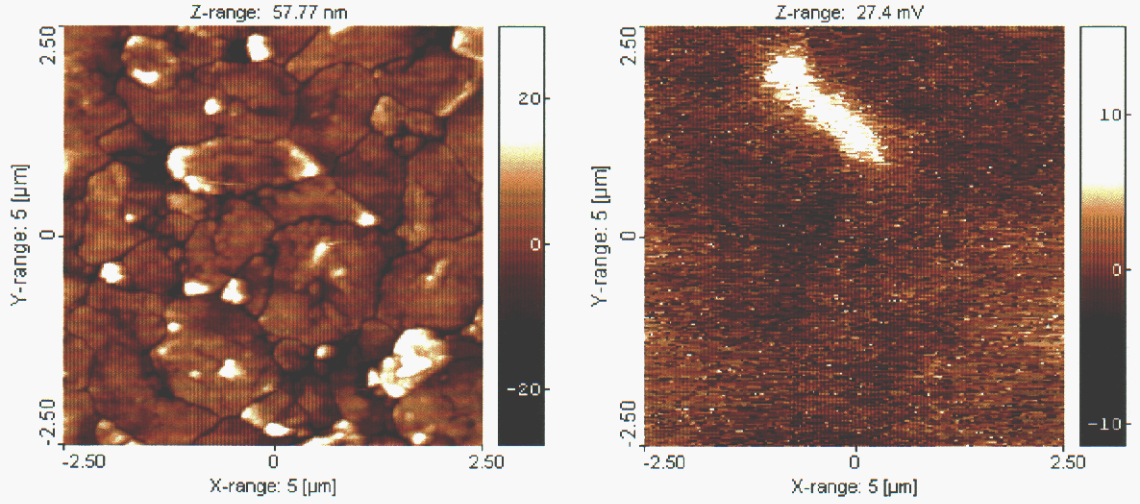

Figure 22. Topographic (a) and surface potential (b) images from a polycrystalline Si surface with $8x10^{13}$ FOTAS molecules•cm^{-2}. A defect region is observed that exhibits a +20 mV potential versus the surrounding region in the upper half of image b).

The topographic image shows the individual Si grains that comprise the chemical vapor deposited Si layer plus more pronounced protruding structures, possibly particles that appear preferentially along the grains boundaries. The total height variation in this 5x5 μm^2 image is almost 60 nm. The surface potential image shows an elongated region of approximately +20 mV higher potential running diagonally downward in the upper half of the image. This potential increase represents approximately 10% of the total potential change measured for this level of FOTAS coverage relative to bare polycrystalline Si (see Fig. 8). This increased potential could be interpreted as an area of 10% lower FOTAS coverage, a region where the average orientation of the FOTAS molecules has become more parallel to the surface, or a position of preferential uptake of an electropositive contaminant species. The size of this region measures 300 to 400 nm in width and less than 2 μm in length. Although such modified regions are not commonly detected in this characterization work, this example does highlight the submicron sensitivity of the SKFM technique on topographically rough surfaces.

SKFM can be used to detect chemical and physical modifications to a FOTAS film on device-level Si substrates. The impact of scanning a Si_3N_4 AFM tip at an approximate normal force of 25 nN on a polycrystalline surface at 60% RH is shown in Figure 23.

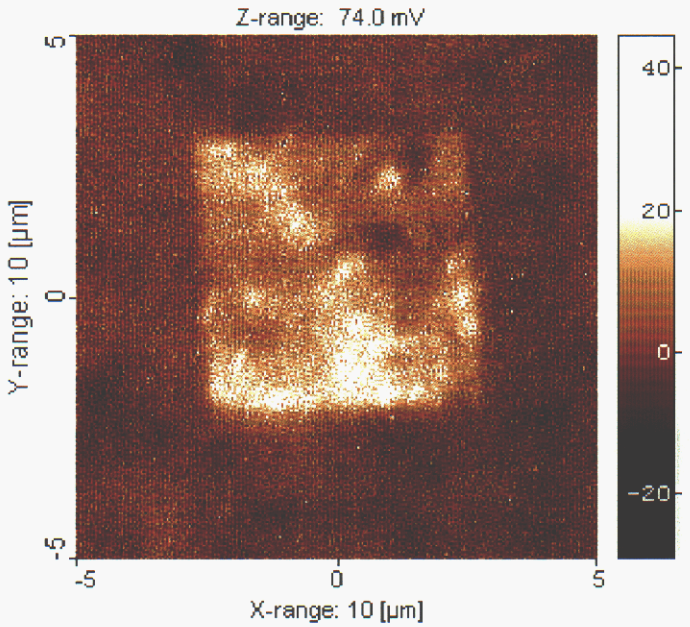

Figure 23. Surface potential image from a polycrystalline Si surface with $2.8x10^{14}$ FOTAS molecules•cm^{-2}. A 5x5 μm^2 region was modified by sanning a Si_3N_4 tip at a normal force of 25 nN in 60% RH in N_2.

A 5x5 μm^2 region was scanned at a 10 $\mu m \cdot s^{-1}$ tip speed. SKFM was used as a subsequent characterization technique to observe the impact of the normal and shear force applied to the sample. The image shows an average potential increase of +15 mV results due to the action of the tip. The potential increase could be due to three different factors: 1) a re-orientation of some fraction of the FOTAS molecules decreasing the vertical projection of the molecular dipole, 2) and displacement of a small fraction of the FOTAS molecules,

or 3) the addition of a surface contaminant (silicones are common tip contaminants) that partially screens the molecular dipole. Further compositional analysis, as discussed in a following section, is required to sort through these possible explanations. The potential is variable with sub-regions exhibiting both higher and lower local values. This effect is most likely the result of local surface topography that contributes to variation in applied local forces during the lithographic phase. Slower tip speeds tend to produce more uniform surface potential distributions. This data shows that rough polycrystalline surfaces (50 nm average height variation) can be probed using the SKFM technique to look for subtle variations in the silane surface film produced by tribological wear.

3.6. Silane Surface Bonding: the Consequences of Varying the Head group Ligands

Considerable disagreement exists within the community of how the silane molecule interacts with the oxide on a Si substrate. Three general perspectives exist which include: 1) predominate siloxane bond formation between the Si head group and surface silanol groups by hydrolysis of a Si-ligand bond followed by loss of H_2O (condensation reaction), 2) preservation of the SiOH group after hydrolysis and resulting H-bonding between the silane and silica silanol groups, and 3) a combination of silane molecules interacting either through siloxane bonds or H-bonds. The local bonding environment is further complicated by the fact that a potentially tri-dentate head group like the tris(dimethylamino)silane might form multiple surface interactions or undergo cross-linking by forming siloxane bridging bonds with adjacent silane molecules. If multiple surface interactions exist for each molecule, it is unlikely that more than one of these could be a silane-surface siloxane bond because the distance between silanol surface moieties is significantly greater than the siloxane bond length. The issue of surface bonding will be discussed in greater detail in another section of this report when considering the attenuated total reflection infrared spectroscopy results. Here, we simply highlight the fact that the monodentate silane (perfluorooctyl)mono(dimethylamino)silane (FOMAS) exhibits a comparable surface concentration as FOTAS at saturation on both polycrystalline Si and Si(100) surfaces. We measure a saturated concentration of 1.9×10^{14} molecules·cm^{-2} (52 Å^2 per molecule) for FOMAS compared to 2.5×10^{14} molecules·cm^{-2} (39 Å^2 per molecule) for FOTAS on polycrystalline Si. The contaminant hydrocarbon concentration found for FOMAS at saturation is comparable to that of FOTAS at 5×10^{13} molecules·cm^{-2}. If cross-linking were prevelant in the FOTAS case, a reasonable expectation would be a combination of significantly higher surface silane concentration coupled with lower contaminant hydrocarbon levels. However, a moderate enhancement (32%) in the silane is measured with no decrease in contaminant levels. The smaller silane concentration for FOMAS could be the result of the steric crowding produced by the two methyl groups bound to the Si head group.

3.7. Model Contaminant Incorporation

The perpetual presence of a residual hydrocarbon in the FOTAS film offers several opportunities to quantify the composition of the film as a function of aging. Although the exact composition of this contaminant surface phase is not known, it must be comprised

of surface active species present in the ambient atmosphere the die is stored in or the module is packaged in. Displacement of FOTAS molecules would result in open surface that could be occupied by these contaminant species. As an example, a phthalate related compound is detected in the SIMS analysis of the FOTAS-coated Si surfaces (see Table 1). An alternative to the direct detection of these species might be through a displacement reaction with a known surface active molecule possessing unique properties that could be tuned to optimize detection by specific characterization techniques. (3-Glycidoxypropyl)trimethoxysilane (GPS) is one such molecule that could serve a chemical marker for FOTAS displacement.

Benkoski has shown that GPS in toluene will readily displace hydrocarbons at the Si surface (20). In addition, the epoxide terminal moiety of this molecule can be reacted with several classes of strong nucleophiles in a classic ring opening mechanism. This active end group allows for the possible bonding of fluorophore molecules to GPS bound to the surface creating an opportunity for optical detection of regions where FOTAS has been displaced due to aging processes. This chemistry follows a solution route and, as such, is not ideal for remote interrogation of module surfaces. However, the concept should be adaptable to a vapor phase process and is worth exploring as a rudimentary step toward a fully integrated, more benign process. The concept also presents an opportunity to investigate film quantification in the presence of a known contaminant.

The first step in exploring this concept is to demonstrate an ability to deposit molecularly smooth GPS films on Si surfaces. Agglomerate formation on the Si surface is a common problem when conducting silane deposition from solution. Agglomerate formation above the nanoscale dimension can be largely eliminated by using low GPS concentrations in the 5 to 50 μM range (0.1 to 1% vol. in anhydrous toluene) for short to moderate deposition times. Figure 24 shows intermittent contact AFM images and the resulting population profiles of agglomerates for GPS deposited on Si(100).

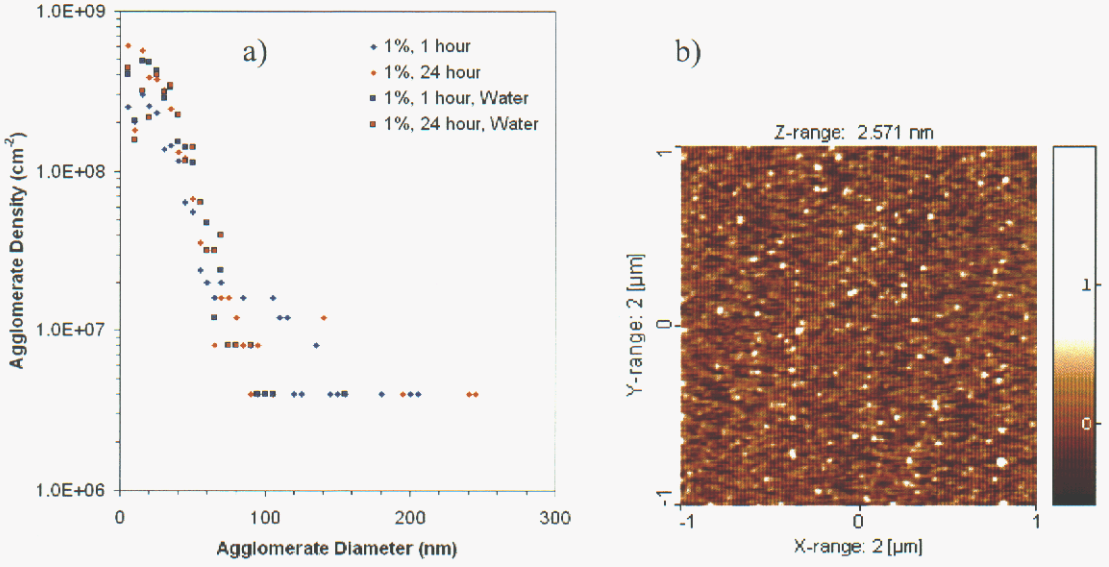

Figure 24. a) Plots of AFM-detected agglomerate density and size as a function of GPS deposition time from a 1% vol. toluene solution onto Si(100). Water indicates a post-deposition 10 minute sonication in Nanopure H_2O. b) Intermittent contact AFM image of a 1 hour, 1% vol. GPS in toluene deposit on Si(100).

Deposition from low concentration solutions results in a distribution of minimum size and low density of agglomerate particles. Sonication in de-ionized water can further reduce the density of these deposition artifacts. Sonication for a 10 minute period was used in the following GPS infill experiments with no detrimental impact on the FOTAS film.

GPS will irreversibly displace hydrocarbon contaminants in a FOTAS film. Monochromatic XPS measurements show the presence of a characteristic ratio of electropositive carbon due to the ether and epoxide carbon atoms to reduced, aliphatic carbon. Figure 25 shows C(1s) spectra for polycrystalline Si with 0, 50 and 100% saturated FOTAS concentrations.

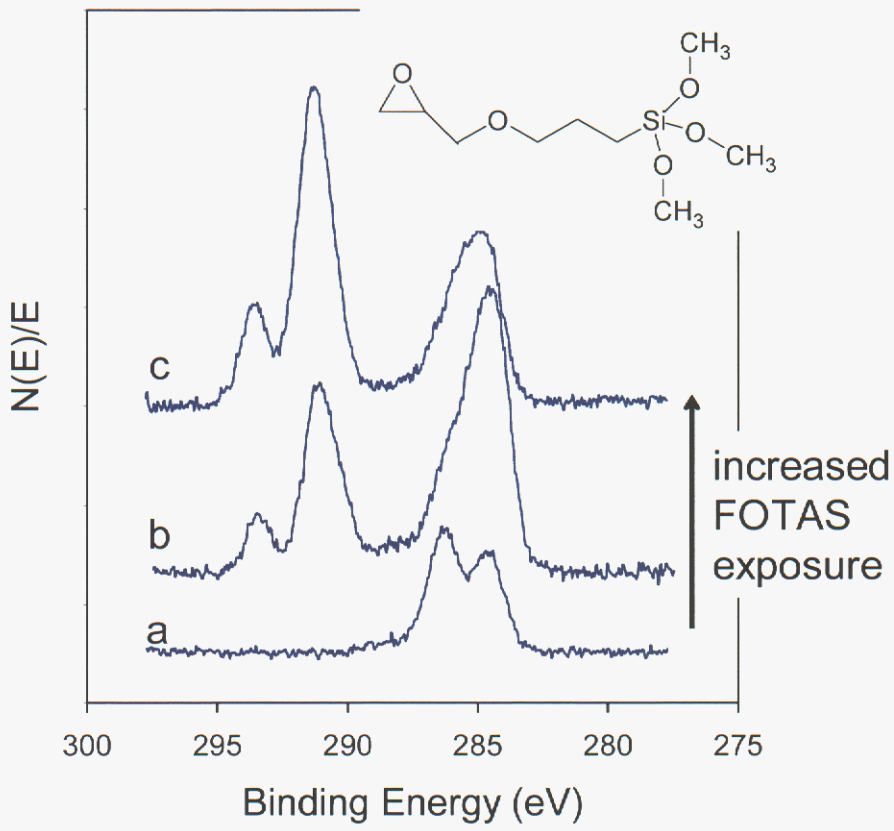

Figure 25. Variation in C(1s) spectra for polycrystalline Si with increasing initial FOTAS coverage exposed to GPS: a) 0%, b) 50% and c) 100% saturation FOTAS coverage. Figure inset shows the chemical structure of the GPS molecule.

In the absence of FOTAS, two C(1s) peaks are observed positioned at 284.6 and 286.3 eV. The lower binding energy peak is due to aliphatic carbon while the higher binding energy peak is consistent with carbon bound to oxygen either as an ether or epoxide. The peak area ratio is 1.25 in contrast to an expected value of 2.0 for the pendant chain of the GPS molecule (see inset to Figure 25). We assume that the Si head group undergoes complete hydrolysis with loss of the methoxy ligands. This lower than expected value can be interpreted to result from only 75% of the hydrocarbon displaced by GPS or post reaction contamination of the surface. Spectra acquired for 50% and 100% FOTAS saturation show a remnant of the ether/epoxide C(1s) as a shoulder on the more dominant aliphatic $^{\beta}C$ and $^{\alpha}C$ peaks due to FOTAS. These results clearly show that GPS in depositing within or on the FOTAS film.

Conducting deposition at various levels of FOTAS film saturation helps quantitatively highlight the role that GPS is playing. The results of this comparison are displayed in Figure 26 which shows that the GPS surface concentration is inversely related to the FOTAS concentration and closely tracks the trend observed for residual hydrocarbon contaminants.

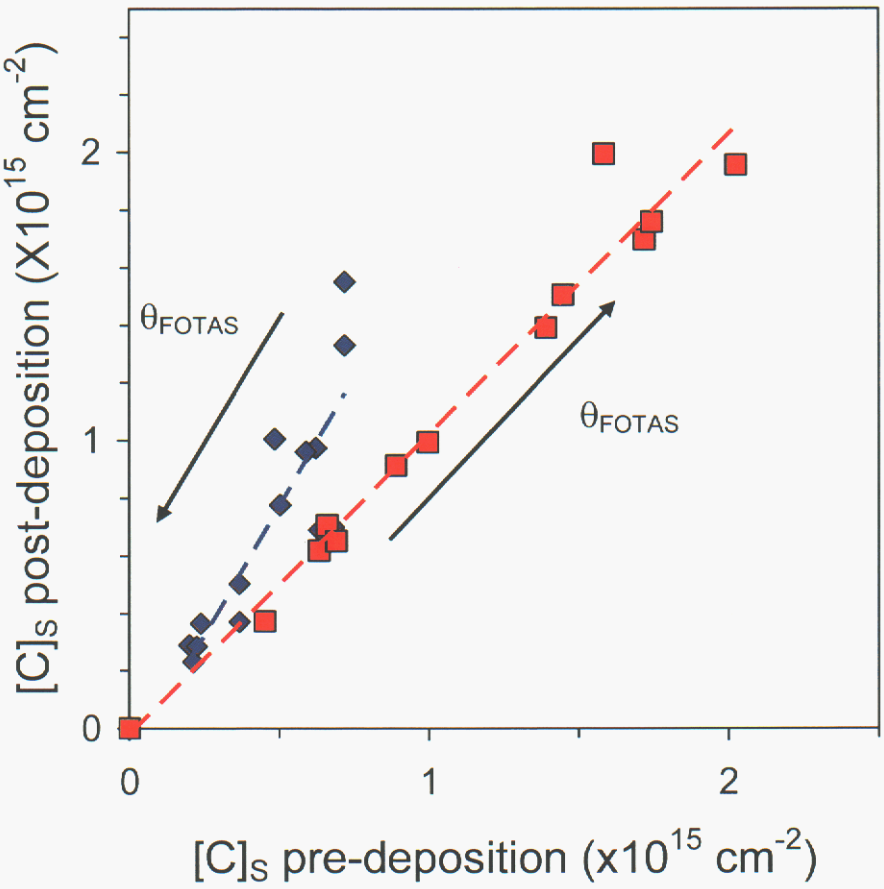

Figure 26. A comparison of the variation in C surface concentration (atoms·cm^{-2}) for FOTAS (■) and GPS (♦) before and after GPS deposition for variable θ_{FOTAS} films (0 to 2.8x10^{14} molec·cm^{-2}) on polycrystalline Si. Arrows indicate the direction of increased θ_{FOTAS}.

This correlation between GPS and contaminants is seen when comparing the carbon atom areal density for non-FOTAS carbon before and after GPS deposition. This comparison is made in Figure 26 with the *before* and *after* deposition FOTAS levels included. Here, we find that a linear relationship exists between GPS and displaced hydrocarbon with a slope of approximately 1.74. So, a C_6 molecule is displacing a population of C_3 and C_4 contaminant molecules. If this latter population contained an equivalent quantity of three and four carbon molecules, then 100% displacement by GPS would be expected to yield a 1.75 increase in total carbon which is what is observed. Equally noteworthy is the fact that the before and after FOTAS carbon density is largely unchanged (slope of 1.04) indicating that FOTAS is neither significantly displaced nor covered.

We conclude from these measurements that GPS exhibits a high efficiency for contaminant displacement within FOTAS films. This chemistry leaves available an active epoxide group to which fluorophore attachment appears to be a possibility. The specific results of optical spectroscopic experiments are discussed in a separate section of this report. However, success in attaching an fluorescent label can be demonstrated using SIMS. GPS-treated FOTAS films can be further exposed to a molecular probe molecule like 5-(4,6-dichlorotriazinyl)aminofluorescein (5-DTAF). This molecule has a secondary

amine which is expected to be reactive toward the epoxide moiety of the GPS molecule at elevated temperature. The FOTAS film can be lithographically patterned to accept the GPS molecule by locally displacing the perfluorinated silane, as shown in the SIMS-derived image and spectra of Figure 27.

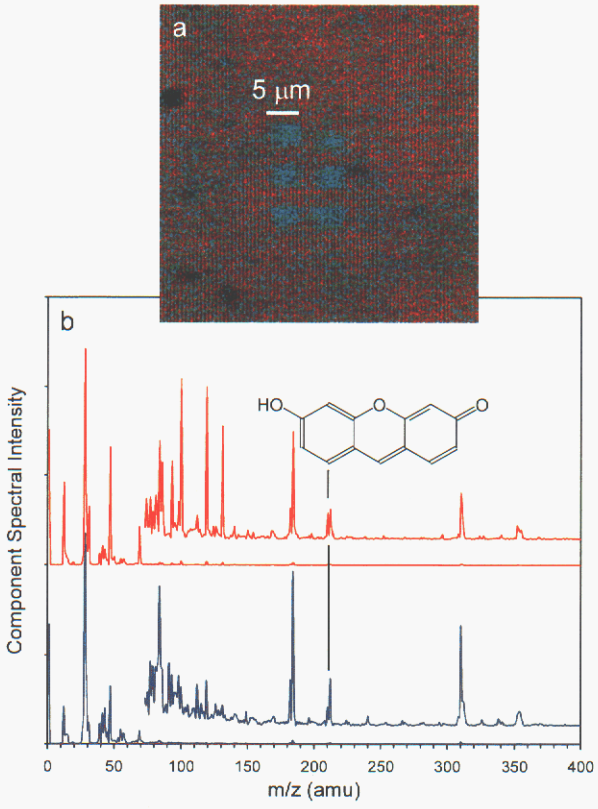

Figure 27. AXSIA-derived SIMS image (a) and component spectra (b) of a lithographically patterned FOTAS film on Si(100). FOTAS has been partially displaced in a 9x9 array of 5x5 µm^2 regions followed by addition of GPS and 5-DTAF.

The original patterned region was a 9x9 array of 5x5 µm^2 squares on a 10 µm pitch. The SIMS image shows evidence of 6 of these regions, indicating changes in the tip-surface interaction over time and a lessening of the intended impact of the lithography. Spectrum A corresponds to the red colored regions in the SIMS image while B corresponds to the aqua colored areas. The lithographic regions contain a significant contribution from spectrum B which exhibits more intense contributions of 39 – 45 amu and 55 – 57 amu secondary ions. These ions are characteristic of fragments produced from the epoxide and ether segments of the GPS molecule. Also of note is the presence of the xanthen-3-one ion (221 amu) of 5-DTAF, the most stable fragment due to its extent of conjugation, as a constituent in the patterned area. The data demonstrates that patterning has been accomplished and indicates that both GPS and DTAF have been deposited with some enhancement in the patterned areas. However, the data also indicates that these molecules are not exclusive to the patterned areas. Attempts to image this patterned area using scanning confocal laser microscopy with Ar ion excitation at 488 nm and 0.25 µm spatial resolution failed to detect the pattern as well as general background fluorescence due to

DTAF. This route toward remote optical detection of FOTAS displacement appears promising, but clearly details of the chemistry need to be resolved to meet minimum optical detection limits.

3.8. Chemical Modification of FOTAS Films to Probe Contaminant Adsorption and Incorporation

The AFM is a suitable platform for conducting localized structural and compositional modifications to a SAM film. A considerable body of work has been published surrounding AFM-based lithographic techniques like nanolithographic patterning, anodic oxidation, nanografting, and dip-pen nanolithography. These techniques are potentially equally applicable to the study of film stability as they are for synthesis purposes.

The combination of a conductive probe tip, moisture, and high electric field will result in localized anodic growth on Si. The threshold for anodic growth for ODTS films on Si(100) has been measured to be +4V (21). FOTAS-coated Si(100) exhibits an equivalent threshold. The relative height increase produced by applying a potential to a Pt tip with respect to the FOTAS-coated Si(100) sample at 35 %RH is shown in Figure 28.

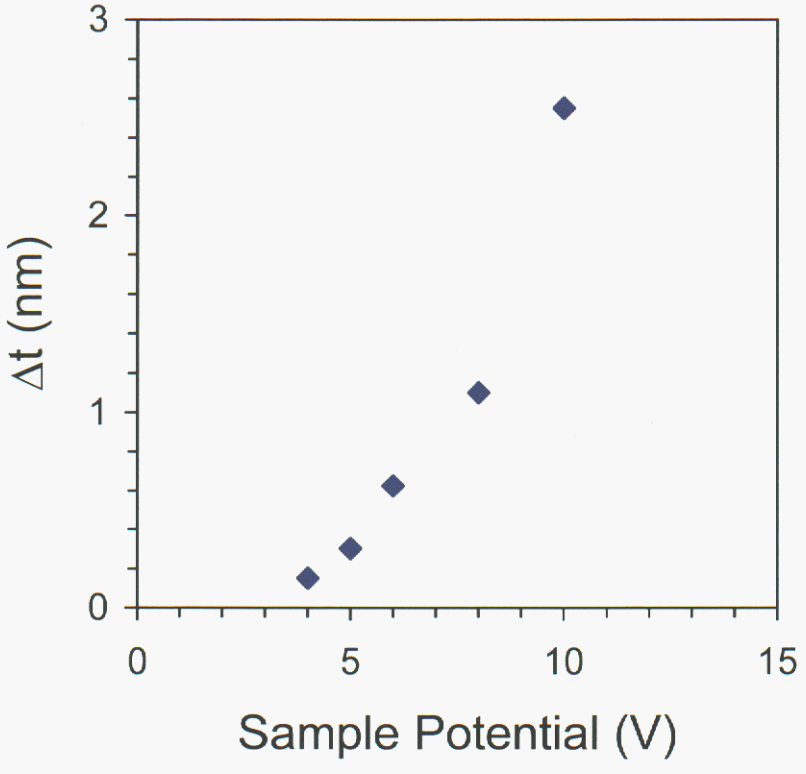

Figure 28. Local topographic change or thickness increase (Δt) observed using an AFM when the Si sample versus Pt cantilever tip potential is varied in N_2 at 35% RH. The thickness increase is a result of local oxide growth at the FOTAS-coated Si(100) surface.

A measurable local topographic change of 0.1 nm is not observed until +4V is applied between sample and tip. This change represents the onset of anodic growth of the oxide and higher potentials produce a characteristic exponential increase expected for local anodization of the Si. Anodization takes place because H_2O penetrates the FOTAS film and OH^- ions are injected into the underlying oxide that the SAM film is bonded to. Topographic changes results because of the larger specific volume of the oxide relative to the Si that generates a local volume increase. Where potentials less than +4 V do not result in oxide growth, changes are observed in lateral forces profiles indicating that chemical changes take place prior to the onset of anodization that alter the forces acting between tip and surface. This variation in lateral force signal is also observed at negative sample potentials. Electric field is capable of producing structural and or chemical changes at the FOTAS-coated Si surface. This sensitivity to field appears to be a method by which mechanism specific, directed aging experiments, like H_2O penetration through the SAM, can be conducted to probe the stability of FOTAS films on Si.

These directed aging studies are conducted within fiduciary indexed arrays (generated by indentation) on Si surfaces so that post-lithographic analysis can be conducted. An example of an array undergoing lithographic modification with a conductive cantilever is shown in Figure 29.

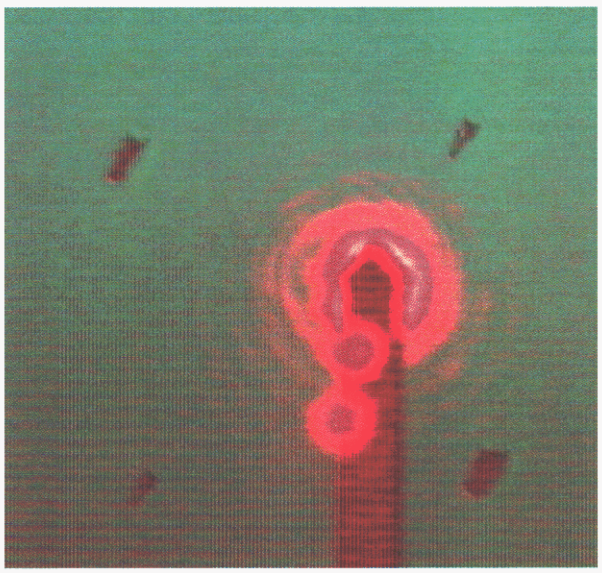

Figure 29. Optical micrograph of a Pt-coated cantilever positioned within an array of fiduciary marks generated on a FOTAS-coated Si sample.

Post-lithographic analysis is conducted both on the AFM (*in situ*) and after removing the sample form the controlled atmosphere chamber of the AFM system. The more useful techniques with which to perform *in situ* analysis are SKFM and phase imaging in intermittent contact mode AFM. *Ex situ* analysis is conducted using TOF-SIMS to provide information about local compositional changes produced by mechanical and electrostatic force of the cantilever tip. Figure 30a shows the analysis results of a directed aging experiment conducted at -10V and 60% RH in N_2 for a FOTAS-coated polycrystalline surface.

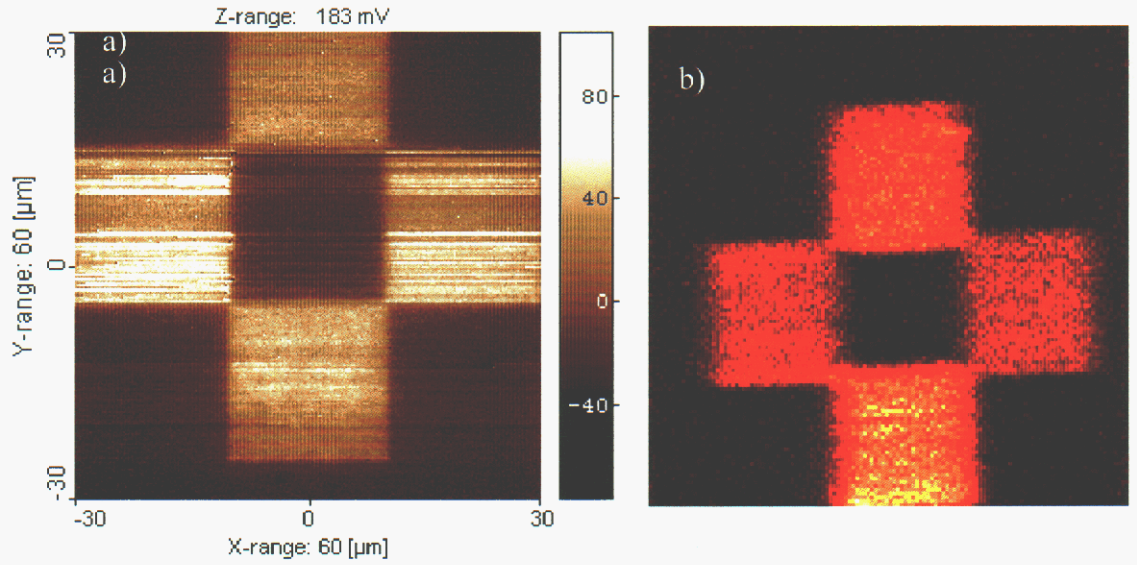

Figure 30. Surface potential image (a) and SIMS-derived image (b) of four 20x20 µm2 regions on FOTAS-coated polycrystalline Si lithographically modified at -10 V sample potential and 60% RH. The total average surface potential increase is +70 mV and the primary constituent in the SIMS image is due to Na^+ secondary ion.

A pattern of four 20x20 μm^2 square regions were generated. SKFM shows a consistent +70 mV increase in potential for the modified areas. This same pattern can be located and analyzed in a SIMS spectrometer. Figure 30b shows the AXSIA-derived results of this analysis where only one of several identified components is displayed. This component is primarily composed of Na and a clear spatial correlation exists between where the tip interacted and where Na signal is enhanced.

A number of lessons are learned from a collection of these experiments. The primary affect of the tip interacting with the FOTAS film under electric field and moisture is the either a displacement or reorientation of molecules at the surface. Evidence of molecular displacement come from SIMS measurements that show a 10% decrease in the FOTAS surface coverage based on the univariate calibration technique discussed previously in this report (SiF^+/Si^+). Additionally, SKFM images of these same lithographic regions show a 12 to 14% increase in the measured surface potential lithographic region. Because potential varies nearly linearly with FOTAS surface coverage, these two numbers are consistent with comparable SAM material loss from the lithographic region. At maximum electrostatic forces (i.e. -10 V sample potential), the degree of displacement is not particularly sensitive to the humidity level with comparable loss values observed from 26 to 60% RH. The role of humidity level may be more strongly coupled to the time necessary to rebuild a water layer on the cantilever tip. More consistent displacement is observed at higher RH values for repetitive patterning. Large negative field is also responsible for driving cations like Na^+ and K^+ into the FOTAS film. The data of Figure 31 is representative of this process. The source of these ionic species is the cantilever tip itself. Figure 31a shows a composite secondary ion image (SIMS) of the underside of the cantilever and the protruding tip.

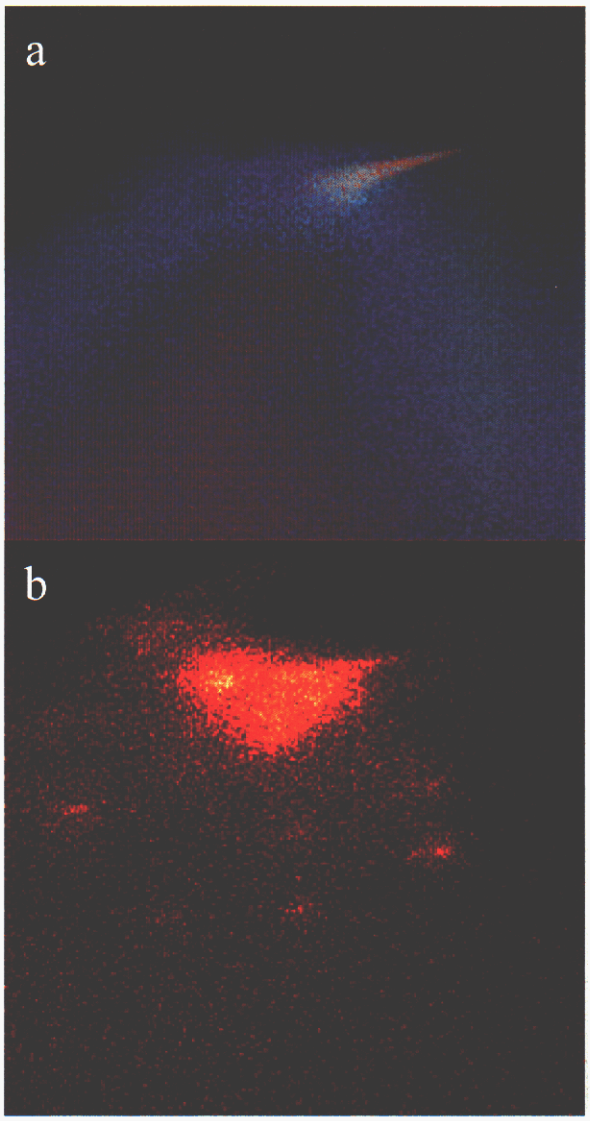

Figure 31. SIMS-derived secondary ion images of a cantilever tip used to lithographically modify FOTAS films on Si at high field and moderate RH: a) composite ion secondary ion image where color denotes compositional variation and b) Na distribution from the same view and perspective. The Na is clustered around along the tip and around the tip base on the cantilever underside.

Na is detected in this measurement and multivariate data analysis shows that it is distributed along the length of the tip and at the tip base on the underside of the cantilever (Figure 31b). Clearly, cations migrate under the influence of field through the medium of a thin H_2O layer, which must coat the Pt tip at 50 to 60% RH, and penetrate the FOTAS film. It is reasonable to expect that these ions carry with them H_2O solvation sphere and that H_2O is also driven into the film.

Direct evidence of H_2O transport into the film has been detected. Figure 32a shows a SIMS-derived 30x30 μm^2 region that was lithographically patterned at +4 V (right at the anodic threshold) at 60% RH in N_2.

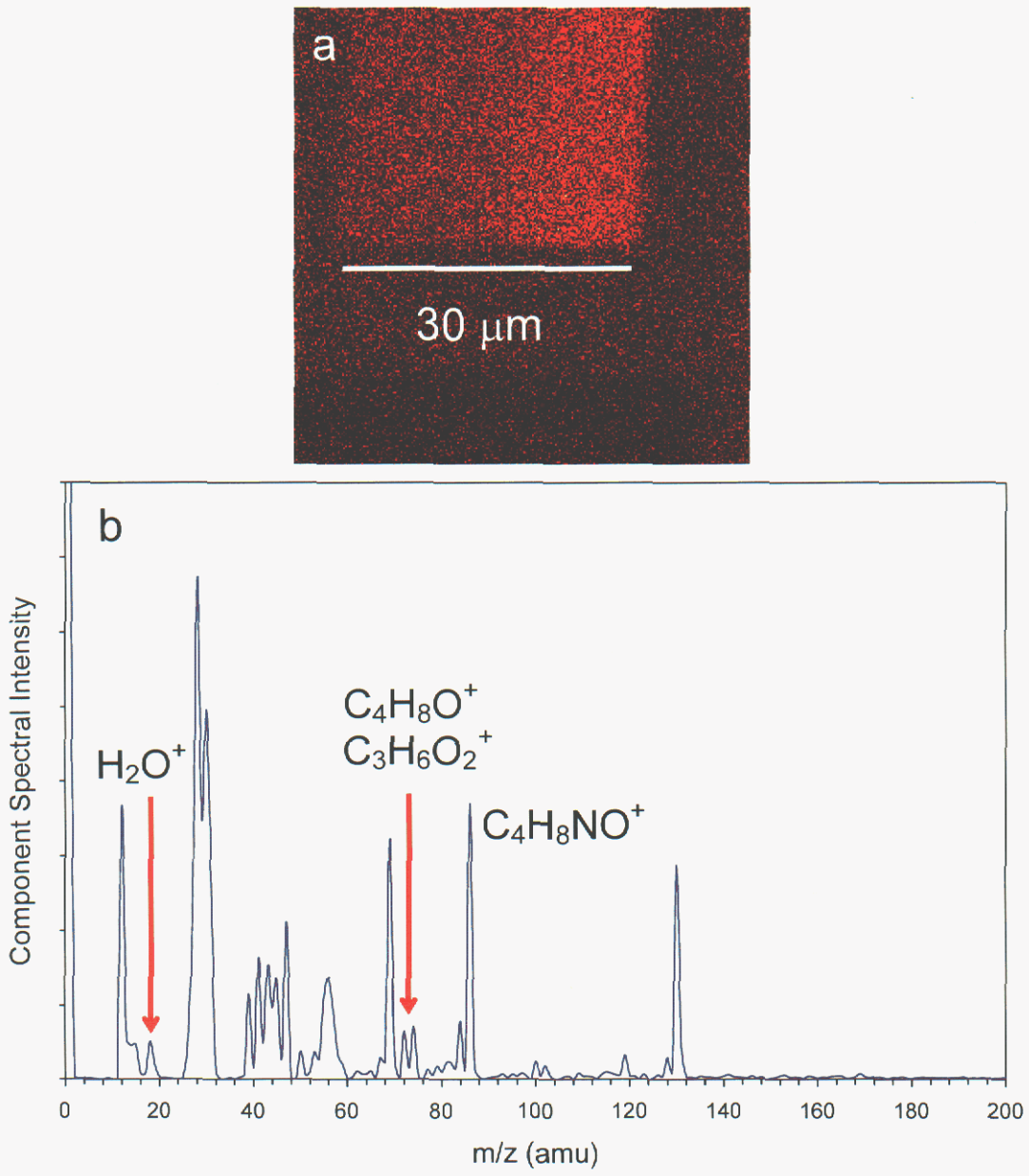

Figure 32. SIMS-derived image (a) and corresponding component mass spectrum (b) of a 30x30 μm² region on FOTAS-coated Si(100) patterned at +4 V and 60% RH in N_2. H_2O incorporation into the FOTAS film is indicated by the appearance of the 18 amu H_2O^+ ion along with some oxidative degradation products.

This AXSIA-derived image represents a region of unique chemical composition. One of the constituent ion detected solely in this modified area is the H_2O^+ ion at 18 amu, as seen in the accompanying mass spectrum for this component in Figure 32b. The detection of H_2O during an ultrahigh vacuum based analysis is a surprising result and suggests a strong interaction between the injected H_2O and the SAM film or the SAM/Si interface. Comparison of the SiF^+/Si^- ratio shows a 2% decrease indicating a much less perturbed FOTAS film composition than levels measured for -10V modification. SKFM

measurements for +4 V modified regions yield smaller potential increases that are typically less than half the magnitude measured at -10 V, also consistent with lower displacement of FOTAS. The results demonstrate the action of a cantilever tip at the FOTAS-coated Si surface at low normal force levels leads to small levels of SAM displacement. Displacement may be facilitated by the presence of H_2O. Electric field serves to drive water and ion transport into the film. Further study will be necessary to determine whether FOTAS displacement is enhanced once water is incorporated at the SAM/Si interface.

3.9. Summary

Techniques were developed during the course of this LDRD project to quantify SAM surface coverage at the MEMS device level. The quantification of Sandia's current VSAM molecule was demonstrated on device-level substrates and at the MEMS device level. Additional, new information pertaining to the composition and structure of these this film is provide using the electron, ion and optical spectroscopic methods developed during the course of this project. In addition, chemical methods were explored as a route to probe nascent and aged film characteristics. Novel scanning probe microscopic methods were also developed to extend the spatial resolution for film characterization. The techniques have been applied at both the device and packaged device levels. We have extended our quantitative capabilities to concurrent projects in an effort to validate our findings and learned knowledge.

4. SAM MAPPING USING FLUORESCENT TAGGANTS

We have investigated means of mapping self-assembled monolayer (SAM) coatings on MEMS devices using photoluminescence (PL) from fluorescent taggants. The SAMs currently in use, FOMAS and FOTAS, are aminosilanes with fluorocarbon chains. The aminosilane end of these molecules bonds to Si-OH groups on silicon surfaces, and the fluorocarbon ends are pendant. There are two potential tagging strategies: positive and negative. Positive tagging seeks to directly tag surface-absorbed FOMAS or FOTAS molecules with a fluorescent probe. Since the fluorocarbon end of these molecules is relatively inert chemically, it would be necessary to utilize the reactivity of the amine groups of the FOMAS/FOTAS molecules for taggant bonding. Since the amine portions of FOMAS and FOTAS may be completely removed as the SAM coatings bond to a silicon substrate and since clustering of pendant fluorocarbon chains on silicon-bound FOMAS and FOTAS molecules might prevent access to any remaining amine groups, we expected a greater likelihood of success using negative tagging.

In negative tagging we bind fluorescent taggants to portions of a silicon surface not covered by SAMs. We have obtained a number of fluorescent taggants and are investigating their ability to bind directly or through an intermediary to a silicon surface. The intermediary is (3-glycidoxypropyl) – trimethoxysilane, or GPS (Figure 33), whose silane end bonds to oxide species on a silicon surface, leaving a reactive epoxide group pendant. GPS is known to displace adventitious hydrocarbons from silicon surfaces (20). The intent is for this intermediary to occupy surface areas not covered by intentionally deposited SAMs and to bond to fluorescent taggants. Infrared analysis of taggant/GPS mixtures showed reaction of the GPS epoxide group at elevated temperatures, suggesting that it is possible to react taggants with GPS.

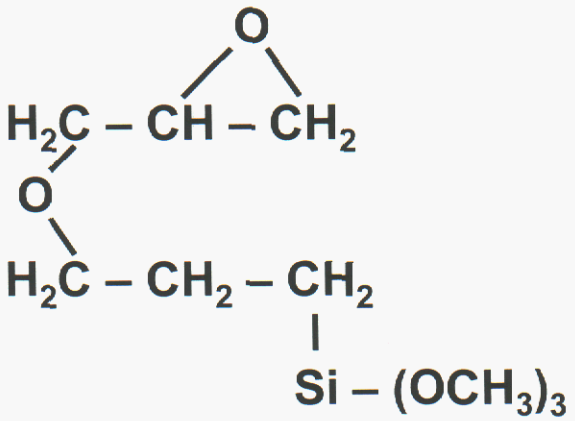

Figure 33. (3-glycidoxypropyl) – trimethoxysilane, or GPS.

Preliminary experiments involving the binding of fluorescent taggants to GPS-coated silicon surfaces showed promise. GPS does not exhibit detectable photoluminescence (PL) with the excitation conditions used in these experiments, but we observed PL characteristic of the taggants. Binding of the fluorescent taggants was carried out as follows:

1. Apply a multiple monolayer coating of GPS to a silicon wafer;
2. dip-coat or drop-coat the silicon with the fluorescent taggant in a solvent;
3. heat the silicon wafer to 100°C for 1 hr to bind the taggant to the GPS; and
4. rinse the silicon wafer with solvent to remove unbound taggant.

In subsequent experiments we applied GPS to only a portion of the silicon wafer's surface, with the intent that the taggant should bind only where the GPS is present. We used two fluorescent dyes, m-dansylaminophenylboronic acid (M-dansyl) and 5-(4,6-dichlorotriazinyl)aminofluorescein (5-DTAF) as the taggants. Various solvents were used to apply the taggant to the silicon wafer. Results are shown for methanol and acetone. GPS does not exhibit detectable photoluminescence (PL) with the excitation conditions used in these experiments. Figure 34-Figure 36 show PL from the partially GPS-coated, taggant-bound silicon wafers.

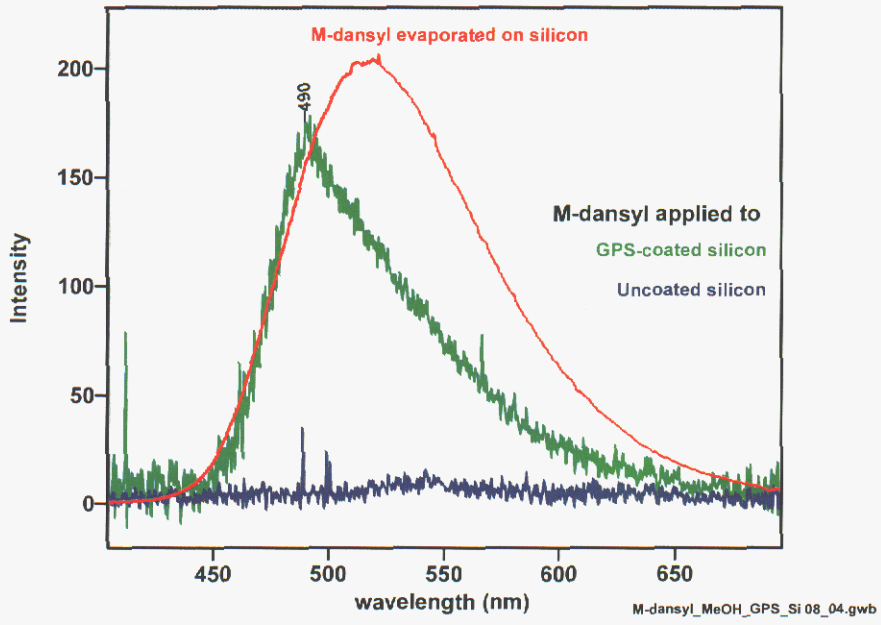

Figure 34. Photoluminescence (337 nm excitation) from partially GPS-coated silicon exposed to M-dansyl in methanol.

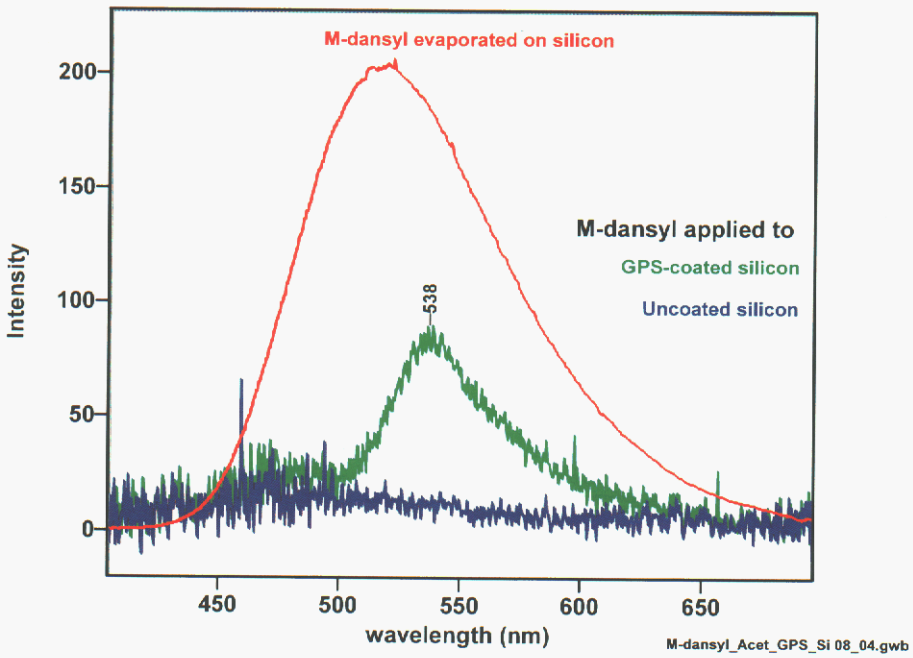

Figure 35. Photoluminescence (337 nm excitation) from partially GPS-coated silicon exposed to M-dansyl in acetone.

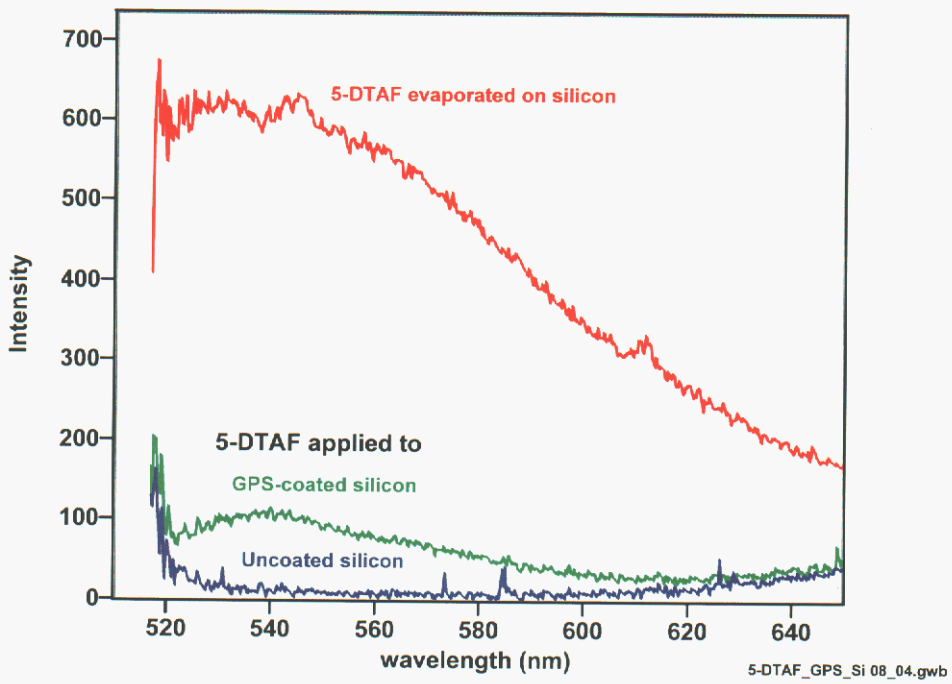

Figure 36. Photoluminescence (492 nm excitation) from partially GPS-coated silicon exposed to 5-DTAF in acetone.

These figures also include spectra of the taggants from samples with relatively thick layers on silicon, which were deposited by evaporating the solvent from drops of taggant-containing solution. The spectra from the thick layers of taggant have been scaled in intensity for comparison with the PL from the taggant-bound, GPS-coated silicon wafers.

For M-dansyl applied with acetone and methanol and for 5-DTAF applied with acetone, PL distinctive of the taggant was observed where silicon had been coated with GPS but not where the GPS is absent. Taggant PL was not observed when 5-DTAF was applied with methanol. In each case where PL was observed on GPS-coated silicon, the PL emission profile is somewhat different from that of the drop-coated and evaporated taggant. These differences are believed to result from reaction of the taggant with GPS and appear to depend on the solvent (compare Figure 34 and Figure 35). These results indicate that a fluorescent taggant can be bound selectively to GPS-coated areas of silicon.

Observing the taggant-bound, GPS-coated silicon wafer surface through a fluorescent microscope reveals areas of concentrated PL, as though either the taggant or GPS is not present in a uniform coating. Topographic AFM images (as in Figure 37) of multilayers of GPS on silicon, deposited by the same protocol as used for the taggant-binding experiments, reveal the presence of bumps or aggregates. Follow-on work would address the issue of GPS or taggant aggregation and would attempt to obtain two-dimensional PL images of fluorescent-bound taggant on surfaces patterned with FOMAS or FOTAS.

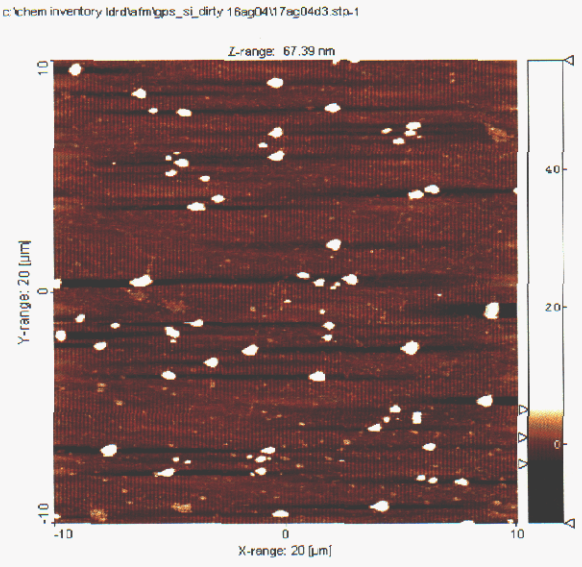

Figure 37. Topographic AFM images of GPS on silicon.

5. PROJECT SUMMARY

Chemical and physical materials-aging processes can significantly degrade the long-term performance and reliability of dormant microsystems, which results from materials interactions that changes both bulk and interfacial properties. The goal was to develop a set analytical strategies and methods to measure the gas and spatially resolved surface chemical inventories in microelectromechanical systems (MEMS).

Molecular level films are a preferred way of tailoring surface properties in (MEMS). Sandia's approach to minimizing inter-surface forces is by using self-assembled monolayers (SAMs) and FOTAS was selected for this work.

Time-of-flight secondary ion mass spectrometric (TOF-SIMS) methods were developed to quantify the surface coverage of FOTAS and generate a unique chemical signature that indicated local SAM displacement. Sophisticated algorithms were developed to extract the useful information from these very large data sets.

X-ray induced photoelectron emission was used to generate the absolute measurement of surface coverage for specially prepared samples that were eventually used to calibrate the TOF-SIMS quantitation algorithms. Monochromatic XPS was demonstrated as a quantitative tool for determining the SAM surface concentration on MEMS device-level substrates.

Atomic force microscopy (AFM) and scanning Kelvin force microscopy (SKFM) techniques were used to investigate subtle variations in the silane surface film produced by tribological wear. Attenuated total reflectance infrared spectroscopy (ATR-IR) was used to explore the structure of VSAM-deposited molecules in a MEMS-like environment.

Finally, methods were developed to determine the hermeticity of MEMS packages using gas analyses. Methods developed are radically different from standard techniques because of the custom hardware used and the pulsed method for gas introduction into the residual gas analyzer. This change enables not only the analysis of nanoliter-sized MEMS packages, but also a rapid way to analyze the gases repetitively in a statistically significant manner (e.g., gas from each package was analyzed dozens of times during a 20 minute time period).

This document is divided into three sections discussing the methods developed for 1) measuring of gases inside of MEMS packages, 2) investigating SAMs coating structures (ATR-IR), and 3) probing surface chemistry and morphology using AFM, SKFM, TOF-SIMS, and XPS.

REFERENCES

(1) Bjorndahl, W. D. Package Size and Epoxy Mass Effects on Package Hermeticity Requirements. 1997; New York, NY, USA : IEEE, 1997:

(2) Lowry, R. K. Sources and Control of Volatile Gases Hazardous to Hermetic Electronic Enclosures. 1999; Reston, VA, USA : IMAPS - Int. Microelectron. & Packaging Soc, 1999:

(3) Narasimhan, T. R. and Trotter, E. H. A Practical Statistical Technique to Improve Seal Integrity and Reliability of Microelectronic Packages. 1997; New York, NY, USA : IEEE, 1997:

(4) Roustan, P. and Revol, D. Residual Gas Analysis: Results Interpretation. Vide-Science Technique et Applications **1995,** *51* (278), 417-&.

(5) Sharma, J. K. N. A. M., Pardeep. A Flowmeter to Determine Complex Volumes and Small Volumes of Glass Tubes Used in Vacuum Gauge Calibrations. Vacuum **1987,** *37* (11/12), 839-842.

(6) Sandia National Laboratories Albuquerque Nm and Thornberg, S. M. *Stepped Linear Piston Displacement Fundamental Leak Calibration System*, 1988;

(7) M. G. Hankins, P. J. R., P. J. Clews, T. M. Mayer, D. R. Wheeler, D. M. Tanner, R. A. Plass. Proc. SPIE **2003,** *4980* 238

(8) Stevens, M. J. Langmuir **1999,** *15* 2773

(9) Scofield, J. H. J. Electron Spectrosc. Relat. Phenom. **1976,** *8* 129

(10) Seah, M. P. *Practical Surface Analysis*, D. Briggs, M. P. S.; Wiley: New York, 1990; 199-201.

(11) H.S. Hansen, S. T., H. Biebuyck. J. Electron Spectrosc. Relat. Phenom. **1992,** *58* 141

(12) D. Barriet, T. R. L. Curr. Opinion Coll. Interfac. Sci. **2003,** *8* 236

(13) I. Luzinov, D. J., A. Liebmann-Vinson, T. Cregger, M.D. Foster, V. V. Tsukruk. Langmuir **2000,** *16* 505

(14) T.M. Mayer, M. P. D. B., N.D. Shinn, P.J. Clews, T.A. Michalske. J. Vac. Sci. Technol. B **2000,** *18* (5), 2433

(15) M.P. Kraft, M. G. Curr. Opinion Coll. Interfac. Sci. **2003,** *8* 243.

(16) Zhuravlev, L. T. Langmuir **1987,** *3* 316.

(17) K. Hayashi, N. S., H. Sugimara, O. Takai, N. Nakagiri. Ultramicroscopy **2002,** *91* 151

(18) S. Howell, D. K., B. Kasibhatla, C.P. Kubiak, D. Janes, R. Reifenberger. Langmuir **2002,** *18* 5120

(19) D.M. Alloway, M. H., D.L. Smith, N.E. Gruhn, A.L. Graham, R. Colorado, V.H. Wysocki, T.R. Lee, P.A. Lee, N.R. Armstrong. J. Phys. Chem. B **2003,** *107* 11690.

(20) J.J. Benkoski, E. J. K., H. Yim, M.S. Kent, J. Hall. Langmuir **2004,** *20* (8), 3246

(21) B. Pignataro, A. L., S. Cataldo, G. Marletta. Mater. Sci. Eng. C **2003,** *23* 7.

Distribution:

5	MS0889	S. M. Thornberg	01825
1	MS0889	J. R. Brown	01825
1	MS0869	T. A. Ordonez	02722
1	MS0888	K. R. Zavadil	01823
1	MS0886	J. A. Ohlhausen	01822
1	MS0632	R. A. Plass	017691
1	MS0889	M. T. Dugger	01824
1	MS0511	F. W. Sexton	01021
1	MS0831	D. M. Tanner	017691
1	MS1411	D. R. Tallant	01822
1	MS1411	M. J. Garcia	01822
1	MS0889	J. W. Braithwaite	01825
1	MS 0887	D. B. Dimos	01800
1	MS 0123	D. L Chavez	01011
2	MS9018	Central Technical Files	8945-1
2	MS0899	Technical Library	4536